

Self-Similarity and Invariance in Phyllotactic Tilings

Patrick Shipman

University of Maryland, Department of Mathematics and
Max Planck Institute for Mathematics in the Sciences
shipman@math.umd.edu

Abstract It has long been noted that Fibonacci or Fibonacci-like sequences and noble numbers appear in the parameters used to describe the arrangement of leaves on plants. These phyllotactic patterns also display a self-similarity in their local description by a Bravais lattice. This paper begins by showing how some classical number-theoretical theorems on the approximation of noble numbers by rational numbers are connected to the idea of self-similarity. These results are then used to compare the Voronoi tessellations associated with the lattices to the (more regular) tilings observed on plants and to construct regular tilings through extensions in Fourier space of lattice-periodic functions. We conclude by showing how these results are relevant to the analysis of PDE models for phyllotaxis.

Keywords: Fibonacci sequence, noble numbers, continued fraction expansions, Voronoi tessellation

1 Introduction

Inspecting a sunflower head such as one of those of Fig. 1, one may notice first the diamond-shaped seeds that tile the disk. Families of spirals catch the eye, and if one counts the numbers of spirals in each family, one typically arrives at successive members of the Fibonacci sequence $1, 1, 2, 3, \dots$. The spiral families seem to blend into each other so that lower members of the sequence are observed near the center of the disk and higher numbers as one works one's way out. Yet, there is a self-similarity in that locally the pattern is nearly the same throughout the disk. Variations of these observations are observed throughout the plant world. Often it is hexagons rather than diamonds that tile, or the planform may be dominated by ridges. Smooth transitions between spiral families may give way to more abrupt transitions that display defects. But, our goal in this paper is to understand the ideal situation in which plant surfaces display nearly regular tilings.

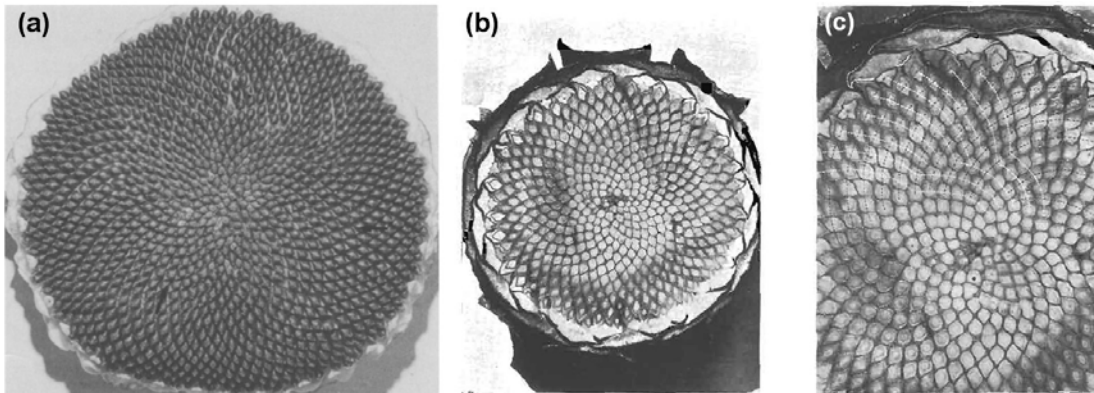


Figure 1: Sunflower seed heads. (a) A seed head of *helianthus hydra*, reproduced from J. H. Palmer [19], with permission from World Scientific. The spiral families come in Fibonacci numbers. (b,c) A seed head of *helianthus annuus*, reproduced from A. H. Church's *On the Relation of Phyllotaxis to Mechanical Laws* [3]. Church refers to this as an *anomalous capitulum* as the spiral families come in the Fibonacci-like sequence $\dots, 11, 18, 29, 47, \dots$ rather than the (classical) Fibonacci sequence. Some of the spirals are marked in (c); note the transition from one family of spirals marked in white to the next.

Phyllotaxis refers to the arrangement of leaves (or analogous elements such as a sunflower's seeds) on a plant. These elements originate in an annular *generative region* surrounding the very tip of a growing plant apex as small bumps called *primordia*. The primordia then grow in size and develop in shape as they move away from the plant tip (due to growth of the apex away from them). But, the angular positions of the primordia typically remain unchanged in this process, so that their relative positions change only in radial spacing. This process of primordium initiation and development occurs on a plant apex with a geometry that varies from a cylinder to a hemisphere to being relative flat [14]. While some investigations of phyllotaxis (notably those of Bravais and Bravais [2] and van Iterson [30]) have been expressed as lattices on cylinders, others (such as Church [3] and Richards [23]) have worked in planar annuli. In the case of a cylinder, the crucial parameter is the radius R , which, in the spherical geometry, can be interpreted as the distance that the primordia form from the very tip of the plant apex. The key element in any model of phyllotaxis that allows for the development of Fibonacci-spiral patterns is the continuous increase of the ratio of R to the (typically constant) size S of newly formed primordia. This ratio takes various forms depending on how primordium size is measured, but it may generally be referred to as the van Iterson parameter. van Iterson himself represented primordia as disks, so that S would be the diameter of a disk. This approach has figured in the work of many authors since [1, 6, 7] and motivates the question of maximal packing, whereby one asks what arrangement of nonoverlapping disks best covers the geometry under consideration [6].

But, how can we understand the non-circular polygonal shapes that seem to tile the entire surface, as observed in Fig. 1? The idea of Voronoi tessellation was introduced to phyllotaxis by Occelli [18], Rivier [24, 25], and Rothen and Koch [27]. Given a set of points in the plane, Voronoi tessellation divides the space into polygons, each containing one of the points. In Section 2.2, we review Voronoi tessellation and how, representing primordia as points, only certain arrangements of primordia give rise to self-similar Voronoi tessellations. In particular, self-similarity requires that the divergence angle of the pattern (defined in Section 2.1) approach a noble number (such as the golden number, as discussed in Section 2.4). Ridley [22] formulates a packing efficiency based on the least-square distance between primordia (again represented by points) and achieves maximal efficiency with noble numbers, and Dixon [4] suggests a measure of the distortion of Voronoi polygons that is minimized by arrangements involving the noble numbers. However, the tilings seen on a plant are typically not Voronoi polygons [11], and Voronoi tessellations are not regular as those observed, for example, in Fig. 1, where roughly the same diamond is repeated throughout. Furthermore, Richards [23] and Williams [31] point out that for a fixed arrangement of primordia, different tilings are possible. A different approach to tiling was introduced in [16, 28, 29], where we show how planforms of diamonds, hexagons, or ridges arise as Fourier-series solutions to partial differential equations corresponding to a biophysical model for primordium formation. This generalizes the study of phyllotaxis by calculating not only the relative positions of points or disks, but rather surfaces that display lattice or lattice-like periodicity, or may be dominated by simple ridges such as those observed on some cacti. In [17], this approach is extended to a biochemical model for phyllotaxis, and we show how the combination of biochemical and biomechanical mechanisms affects the tiling shapes.

The aim of this paper is to phrase the number-theoretical ideas relevant to phyllotaxis in terms of symmetries that allow for regular tilings and have applications in the analysis of PDE models and also to compare the results with Voronoi tessellations. The paper is organized as follows: In Section 2, we review how the position of leaf centers form local lattices described by a basis matrix Ω and present a new derivation of how Fibonacci sequences and noble numbers arise in phyllotaxis by considering a self-similarity relation on the matrix Ω as the van Iterson parameter changes. This leads to connections with classical number-theoretical results on the approximation of irrational numbers by rational numbers, which are summarized in Proposition 2. Even though Voronoi tiles do not give regular tilings, we show how they underlie nearly regular tilings in that they correspond to the dominant Fourier modes of a regular pattern. We then extend the idea of self-similarity developed in Section 2 to one of invariance by showing how certain properties of the lattice and the tiling are independent of the van Iterson parameter. Finally, we show how various planforms consistent with a single underlying lattice can arise from varying a metric on the surface and relate this approach to the question of maximal packing. The use of lattice-periodic functions in Section 3 is motivated by Fourier analysis of PDE models for phyllotactic pattern formation [28, 29], and in Section 4 we briefly review this approach and show how the results of Sections 2 and 3 might inform the PDE analysis. The key message here is that the symmetries discussed in the previous sections can contribute to the analysis of PDE models.

2 Cylindrical Lattices

Phyllotactic patterns are typically locally lattices, and we begin in Section 2.1 by reviewing the notation for lattices on cylinders and a basis matrix Ω as presented in [28, 29]. Section 2.2 translates these results to an annulus in the plane and reviews the idea of a Voronoi tessellation. In Section 2.3, Fibonacci-like sequences of basis matrices Ω_ν are studied to provide a new derivation of why noble numbers lead to self-similarity, and in Section 2.4 classical results of number theory on the approximation of noble numbers by rational numbers motivate a proposition on the limiting values of the entries of Ω_ν . Finally, rhombic lattices are briefly discussed in Section 2.5.

2.1 Coordinates and Bases

A Bravais lattice \mathbb{L} in \mathbb{R}^2 consists of all integer combinations $z_1\vec{v} + z_2\vec{w}$ of vectors $\vec{v}, \vec{w} \in \mathbb{R}^2$, $(z_1, z_2) \in \mathbb{Z}^2$. The lattice is periodic in $\vec{u} \in \mathbb{R}^2$ if $\vec{w} + \vec{u} \in \mathbb{L}$ for all $\vec{w} \in L$. Such a lattice can be rolled onto a cylinder of circumference $2\pi R = k\|\vec{u}\|$ for $k \in \mathbb{N}$. We will consider cylindrical lattices of the form

$$\mathbb{L}(\lambda, R, d, g) = \left\{ z_1(\lambda, 2\pi R d) + z_2 \left(0, \frac{2\pi R}{g} \right) : (z_1, z_2) \in \mathbb{Z}^2 \right\},$$

where $\lambda \in \mathbb{R}^+$, $g \in \mathbb{N}$, and $d \in [0, 1]$. \mathbb{L} can be thought of as a $(0, \frac{2\pi R}{g})$ -periodic lattice in \mathbb{R}^2 or as a lattice on a cylinder of radius R .

The vectors $\vec{\omega}_{\lambda, d} = (\lambda, 2\pi R d)$ and $\vec{\omega}_g = (0, \frac{2\pi R}{g})$ form one basis for \mathbb{L} . All other bases are found by taking the linear combinations

$$\begin{pmatrix} \alpha & \beta \\ \gamma & \delta \end{pmatrix} \begin{pmatrix} \lambda & 2\pi R d \\ 0 & \frac{2\pi R}{g} \end{pmatrix} = \begin{pmatrix} \lambda\alpha & 2\pi(d\alpha + \frac{\beta}{g}) \\ \lambda\gamma & 2\pi(d\gamma + \frac{\delta}{g}) \end{pmatrix},$$

where $\alpha, \beta, \delta, \gamma \in \mathbb{Z}$, and $\alpha\delta - \beta\gamma = \pm 1$. Setting $m \doteq g\alpha, n \doteq g\gamma, p \doteq \delta, q \doteq \beta$, this means that all bases of $\mathbb{L}(\lambda, R, d, g)$ are given by $\vec{\omega}_m, \vec{\omega}_n$, where $m, n \in \mathbb{Z}$, $pm - qn = \pm g = \pm \gcd(m, n)$, and

$$\Omega_{(m,n)}(\lambda, R, d, g) \doteq \begin{pmatrix} \vec{\omega}_n \\ \vec{\omega}_m \end{pmatrix} \doteq \frac{1}{g} \begin{pmatrix} \lambda n & 2\pi R(nd - p) \\ \lambda m & 2\pi R(md - q) \end{pmatrix}.$$

The matrix Ω depends on four parameters λ, R, d, g that determine the lattice $\mathbb{L}(\lambda, R, d, g)$ and four parameters m, n, p, q related by $pm - qn = \pm \gcd(m, n) = \pm g$ which choose a basis for \mathbb{L} .

For any choice of m, n and p, q such that $pm - nq = \pm g$, $(p + kn)m - (q + km)n = \pm g$ for any integer k . Thinking of \mathbb{L} as a lattice on a cylinder $[0, \infty) \times (-\pi R, \pi R)$, an ideal choice of p, q is one for which

$$-\pi R < \frac{2\pi R}{g}(md - p), \quad \frac{2\pi R}{g}(nd - q) < \pi R.$$

Rewritten, this condition is that

$$\left| \frac{p}{m} - d \right| < \frac{g}{2m}, \quad \left| \frac{q}{n} - d \right| < \frac{g}{2n}.$$

This says that both $\frac{p}{m}$ and $\frac{q}{n}$ should be good approximations of d . For arbitrary $m, n \in \mathbb{N}$ and d , it is not always possible to find p, q that satisfy these conditions. (Try, for example, $m = 6, n = 7, d = \frac{3}{8}$.) One of the goals of this paper is to show how classical theorems on the approximation of irrational numbers (such as an irrational choice of d) by rational numbers relate to special choices of m, n, p, q, d that allow for self-similarity in cylindrical lattices in the annular geometry as described in Section 2.2.

The area A associated with each point in the lattice $\mathbb{L}(\lambda, R, d, g)$ is defined to be the determinant of Ω ;

$$A \doteq \det \Omega = 2\pi R \frac{\lambda}{g}.$$

Solving this last expression for λ , we can restate the matrix Ω as a function of A, R, d, g ;

$$\Omega_{(m,n)}(A, R, d, g) = \begin{pmatrix} \frac{A}{2\pi R} n & \frac{2\pi R}{g}(nd - p) \\ \frac{A}{2\pi R} m & \frac{2\pi R}{g}(md - q) \end{pmatrix}.$$

Defining $\Gamma \doteq \frac{2\pi R}{\sqrt{A}}$, we arrive at our final form for Ω , namely

$$\Omega_{(m,n)}(A, \Gamma, d, g) = \sqrt{A} \begin{pmatrix} \frac{n}{\Gamma} & \frac{\Gamma}{g}(nd - p) \\ \frac{m}{\Gamma} & \frac{\Gamma}{g}(md - q) \end{pmatrix}.$$

The parameter Γ our version of the van Iterson parameter. We will often in the following also write a cylindrical lattice as $\mathbb{L} = \mathbb{L}(A, \Gamma, d, g)$.

Growth of cylinder in radius from Γ to $\Gamma\Gamma'$ or growth in the lattice from A to AA' is expressed by

$$\Omega_{(m,n)}(AA', \Gamma\Gamma', d, g) = \Omega_{(m,n)}(A, \Gamma, d, g)G(A', \Gamma'),$$

where

$$G(A', \Gamma') \doteq \sqrt{A'} \begin{pmatrix} \frac{1}{\Gamma'} & 0 \\ 0 & \Gamma' \end{pmatrix}.$$

2.2 Cylindrical Lattices in the Planar Annulus

The patterns that we observe on, for example, sunflowers are topologically cylindrical (upon removing the center point, which does not belong to any tile), but geometrically closer to annuli in the plane. These patterns display cylindrical lattices in that the positions of seeds or analogous elements (with radial distance measured in arclength along the curved region) are given by

$$\left(f(j) \cos\left(2\pi dj + \frac{2\pi}{g}k\right), f(j) \sin\left(2\pi dj + \frac{2\pi}{g}k\right) \right),$$

where $f(j)$ is typically approximately $f(j) = f_1(j) = \hat{\lambda}^j$ or $f(j) = f_2(j) = \sqrt{j\hat{\lambda}}$. The parameter d will depend on j , but in many cases it can be approximated by a constant and it typically approaches a constant for large j . The (r, α) -coordinates of the seed centers are thus approximately a cylindrical lattice $\mathbb{L}(\lambda, R = 1, d, g)$. Since many plants display the function $f_1(j)$, the parameter λ is typically called the plastochrone ratio.

For a pattern described by the function f_2 , the seeds will be of equal area. To show this, let us translate our results on cylindrical lattices in the plane to the disk by finding an equiareal transformation from the plane to the disk. An equiareal transformation T is one for which the area of any set Σ of points in the domain is equal to the area of the image of Σ under T . Denoting the coordinates of the plane in which the cylindrical lattice $\mathbb{L}(\lambda, R = 1, d, g)$ lies by (s, θ) (R is taken to be 1 so that the second coordinate can be considered as an angle in $(-\pi, \pi)$) and the coordinates of the plane in which the disk lies by (x, y) , we seek a transformation of the form

$$(x, y) = T'(s, \theta) = (f(s) \cos \theta, f(s) \sin \theta), \quad s \geq 0, \theta \in (-\pi, \pi),$$

so that, in polar coordinates (r, α) , points in the (x, y) -plane are given by

$$(r, \alpha) = \tilde{T}'(s, \theta) = (f(s), \theta).$$

The Jacobian of T' is

$$J_{T'} = \begin{pmatrix} f'(s) \cos \theta & -f(s) \sin \theta \\ f'(s) \sin \theta & f(s) \cos \theta \end{pmatrix},$$

and $\det J_{T'} = f'(s)f(s)$. Solving the equation $f'(s)f(s) = A'$ for $f(s)$, where A' is a given constant, we find that $f(s) = \sqrt{2A's + s_0}$. Here, s_0 is the image under T' of the line $(s = 0, \theta)$. The transformation

$$T(s, \theta) = \left(\sqrt{2A's + s_0} \cos \theta, \sqrt{2A's + s_0} \sin \theta \right)$$

is thus equiareal if $A' = 1$. For $s_0 = 0$, the Jacobian J_T is

$$J_T = \begin{pmatrix} \sqrt{\frac{A'}{2s}} \cos \theta & -\sqrt{2A's} \sin \theta \\ \sqrt{\frac{A'}{2s}} \sin \theta & \sqrt{2A's} \cos \theta \end{pmatrix} = \begin{pmatrix} \cos \theta & -\sin \theta \\ \sin \theta & \cos \theta \end{pmatrix} G(A', \sqrt{2s}).$$

Much of the rest of this paper can be motivated by considering two examples of the image in the annulus of a cylindrical lattice \mathbb{L} in the (s, θ) -plane, as suggested by Rothen and Koch [27]. The images of the lattices $\mathbb{L}_i(A, \Gamma, d_i, g)$ for $A = \Gamma = g = 1$, $d_1 = \frac{3}{8}$, $d_2 = \frac{1}{2}(3 - \sqrt{5})$, are respectively plotted in Fig. 2 (a,b) along with the associated Voronoi polygons. The Voronoi polygon associated with a point P_i in a collection P of points in the plane consists of all points in the plane that are closer to P_i than any other point in P . The two values of d differ by less than 0.00697, but the two pictures are dramatically different. One difference is in the shapes of the Voronoi polygons, all of which are of approximately equal area. For $d = \frac{3}{8}$, the polygons are more and more azimuthally stretched farther from the origin, whereas for $d = \frac{1}{2}(3 - \sqrt{5})$, they remain rough approximations of circles. Another difference becomes apparent when examining the neighbors of a given polygon. The points in Fig. 2 are numbered according to their distance from the origin. In Fig. 2 (a), the number in any polygon differs from the numbers in the neighboring polygons by 3, 5, or 8. In Fig. 2 (b), the difference are three consecutive members of the Fibonacci sequence 1, 1, 2, 3, 5, 8, 13, \dots , with transitions to higher numbers as one moves farther from the origin. It will become apparent that the contrast between these two examples is not merely due to the fact that one value of d is rational and the other is irrational. In the following, we will calculate the values of d that allow Voronoi tessellations such as that in Fig. 2 (b). Our clue to understanding self-similarity is the appearance of the increasing members of the Fibonacci sequence for the case $d = \frac{1}{2}(3 - \sqrt{5})$.

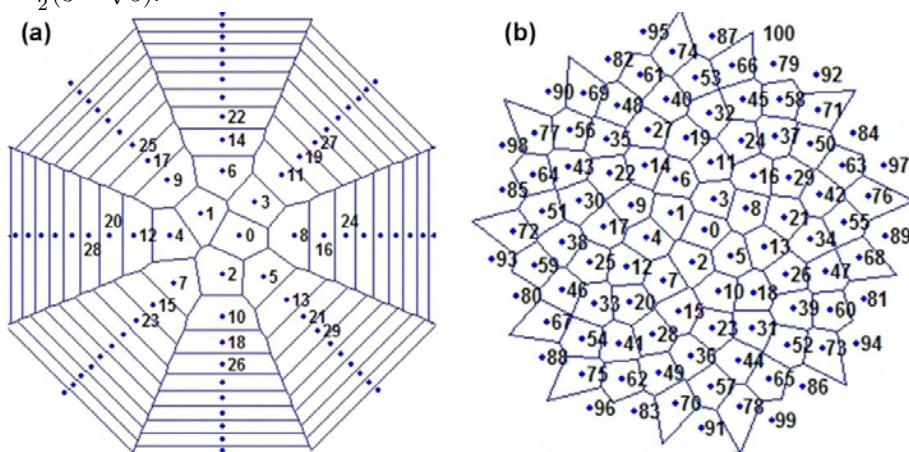


Figure 2: The image, under the transformation T , of the cylindrical lattices (a) $\mathbb{L}(A = 1, \Gamma = 1, d = \frac{3}{8}, g = 1)$, and (b) $\mathbb{L}(A = 1, \Gamma = 1, d = \frac{1}{2}(3 - \sqrt{5}), g = 1)$. The points are numbered according to their distance from the origin. Also plotted are the corresponding Voronoi polygons.

2.3 Fibonacci-like sequences of lattice vectors

Given $\vec{x}_0, \vec{x}_1 \in \mathbb{R}^n$, define a Fibonacci-like sequence by $\vec{x}_{\nu+1} = \vec{x}_\nu + \vec{x}_{\nu-1}$. A key to uncovering many properties of this sequence is the Fibonacci Q -matrix which expresses the recursion relation in matrix form;

$$\text{for } Q = \begin{pmatrix} 1 & 1 \\ 1 & 0 \end{pmatrix}, \quad \begin{pmatrix} \vec{x}_{\nu+1} \\ \vec{x}_\nu \end{pmatrix} = Q^\nu \begin{pmatrix} \vec{x}_1 \\ \vec{x}_0 \end{pmatrix}. \quad (1)$$

Diagonalization of the Q -matrix yields the relation $Q^\nu = MD^\nu M^{-1}$, where

$$M = \begin{pmatrix} \phi_+ & \phi_- \\ 1 & 1 \end{pmatrix}, \quad D = \begin{pmatrix} \phi_+ & 0 \\ 0 & \phi_- \end{pmatrix},$$

and $\phi_\pm = \frac{1 \pm \sqrt{5}}{2}$ are the roots of $\eta^2 - \eta - 1 = 0$. Then, (1) is rewritten as

$$\begin{pmatrix} \vec{x}_{\nu+1} \\ \vec{x}_\nu \end{pmatrix} = Q^\nu \begin{pmatrix} \vec{x}_1 \\ \vec{x}_0 \end{pmatrix} = \frac{1}{\sqrt{5}} \begin{pmatrix} \phi_+^{\nu+1} - \phi_-^{\nu+1} & \phi_+^\nu - \phi_-^\nu \\ \phi_+^\nu - \phi_-^\nu & \phi_+^{\nu-1} - \phi_-^{\nu-1} \end{pmatrix} \begin{pmatrix} \vec{x}_1 \\ \vec{x}_0 \end{pmatrix}.$$

This gives *Binet's formula*

$$\vec{x}_\nu = \frac{1}{\sqrt{5}} [(\phi_+^\nu - \phi_-^\nu)\vec{x}_1 + (\phi_+^{\nu-1} - \phi_-^{\nu-1})\vec{x}_0]. \quad (2)$$

Motivated by our observations of cylindrical lattices in the annulus, we define a sequence Ω_ν of lattice basis matrices. Ω_1 is defined by the four lattice constants A, Γ, d, g and integers m_0, m_1, q_0, q_1 such that $q_1 m_0 - q_0 m_1 = \gcd(m_0, m_1) = g$. $\Omega_1(A, \Gamma, d)$ will be understood within the context of given integers g, m_0, m_1, q_0, q_1 (so that we write it only as a function of A, Γ, d) and is defined by

$$\Omega_1(A, \Gamma, d) \doteq \sqrt{A} \begin{pmatrix} \frac{m_1}{\Gamma} & \frac{\Gamma}{g}(m_1 d - q_1) \\ \frac{m_0}{\Gamma} & \frac{\Gamma}{g}(m_0 d - q_0) \end{pmatrix}.$$

The sequence Ω_ν is then defined by

$$\Omega_\nu \doteq Q \Omega_{\nu-1} \quad \text{for } \nu > 1.$$

Choosing $\vec{x}_0 = (q_0, m_0)$, $\vec{x}_1 = (q_1, m_1)$ in (1), sequences $\{q_\nu\}$, $\{m_\nu\}$ are given by

$$\begin{pmatrix} q_{\nu+1} & m_{\nu+1} \\ q_\nu & m_\nu \end{pmatrix} = Q^\nu \begin{pmatrix} q_1 & m_1 \\ q_0 & m_0 \end{pmatrix}.$$

Noting that $\det Q^\nu = (-1)^\nu$ and taking the determinant of both sides of this last expression yields the relation

$$q_{\nu+1} m_\nu - q_\nu m_{\nu+1} = (-1)^\nu (q_1 m_0 - q_0 m_1) = (-1)^\nu g.$$

Thus,

$$\Omega_\nu(A, \Gamma, d) = \sqrt{A} \begin{pmatrix} \frac{m_\nu}{\Gamma} & \frac{\Gamma}{g}(m_\nu d - q_\nu) \\ \frac{m_{\nu-1}}{\Gamma} & \frac{\Gamma}{g}(m_{\nu-1} d - q_{\nu-1}) \end{pmatrix},$$

where $g = q_1 m_0 - q_0 m_1 = (-1)^\nu (q_{\nu+1} m_\nu - q_\nu m_{\nu+1})$.

The eigenvectors of Q are $(\phi_+, 1)^T$ (with eigenvalue ϕ_+) and $(\phi_-, 1)^T$ (with eigenvalue ϕ_-). Since $\phi_+ > 1$ and $|\phi_-| < 1$, for $x_0, x_1 \in \mathbb{R}$, $|x_n| \rightarrow \infty$ unless the vector $(x_1, x_0)^T$ lies in the ϕ_- -eigenspace, or, equivalently, unless $x_1/x_0 = \phi_-$. The second column of Ω_ν is in the ϕ_- -eigenspace of Q if $\frac{m_\nu d - q_\nu}{m_{\nu-1} d - q_{\nu-1}} = \phi_-$; that is, if

$$d = \frac{q_{\nu-1} + q_\nu \phi_+}{m_{\nu-1} + m_\nu \phi_+}.$$

Like $g = (-1)^\nu (q_{\nu+1} m_\nu - q_\nu m_{\nu+1})$, this last expression turns out to be independent of ν ;

Proposition 1: Given two Fibonacci-like sequences of real numbers q_ν and m_ν generated by q_0, q_1 and m_0, m_1 respectively,

$$\frac{q_\nu + q_{\nu+1} \phi_+}{m_\nu + m_{\nu+1} \phi_+} = \frac{q_0 + q_1 \phi_+}{m_0 + m_1 \phi_+}$$

for all $\nu \in \mathbb{N}$.

Proof: The Q -matrix has left-eigenvector $(\phi_+, 1)$ with eigenvalue ϕ_+ . On the one hand then,

$$(\phi_+, 1) \begin{pmatrix} 1 & 1 \\ 1 & 0 \end{pmatrix}^\nu \begin{pmatrix} q_1 & m_1 \\ q_0 & m_0 \end{pmatrix} = \phi_+^\nu (\phi_+, 1) \begin{pmatrix} q_1 & m_1 \\ q_0 & m_0 \end{pmatrix} = \phi_+^\nu (q_0 + q_1 \phi_+, m_0 + m_1 \phi_+).$$

On the other hand,

$$(\phi_+, 1) \begin{pmatrix} 1 & 1 \\ 1 & 0 \end{pmatrix}^\nu \begin{pmatrix} q_1 & m_1 \\ q_0 & m_0 \end{pmatrix} = (\phi_+, 1) \begin{pmatrix} q_{\nu+1} & m_{\nu+1} \\ q_\nu & m_\nu \end{pmatrix} = (q_\nu + q_{\nu+1} \phi_+, m_\nu + m_{\nu+1} \phi_+).$$

Equating the two computations, we find that

$$\frac{\phi_+^\nu}{\phi_+^\nu} \frac{q_0 + q_1 \phi_+}{m_0 + m_1 \phi_+} = \frac{q_\nu + q_{\nu+1} \phi_+}{m_\nu + m_{\nu+1} \phi_+}.$$

■

Defining $\hat{d}(m_0, m_1, q_0, q_1) = \frac{q_0 + q_1 \phi_+}{m_0 + m_1 \phi_+}$, we have shown that for all $\nu \in \mathbb{N}$,

$$\frac{m_{\nu+1} \hat{d} - q_{\nu+1}}{m_\nu \hat{d} - q_\nu} = \phi_-,$$

and the second column of the matrix

$$\hat{\Omega}_\nu(A, \Gamma) = \Omega_\nu(A, \Gamma, d = \hat{d})$$

lies in the ϕ_- -eigenspace of Q .

We now have the tools to prove the relations

$$Q\hat{\Omega}_\nu(A, \Gamma)G(1, \phi_+) \simeq \hat{\Omega}_\nu(A, \Gamma) \begin{pmatrix} 1 & 0 \\ 0 & -1 \end{pmatrix},$$

and

$$Q^2\hat{\Omega}_\nu(A, \Gamma)G(1, \phi_+^2) \simeq \hat{\Omega}_\nu(A, \Gamma),$$

which express self-similarity in that growth in Γ by a multiplicative factor ϕ_+ , accompanied by a change of basis through Q , preserves the lattice up to a change in orientation. The calculation of the relations is as follows:

$$\begin{aligned} Q\hat{\Omega}_\nu G(1, \phi_+) &= Q\sqrt{A} \begin{pmatrix} \frac{m_\nu}{\Gamma} & \frac{\Gamma}{g}(m_\nu d - q_\nu) \\ \frac{m_{\nu-1}}{\Gamma} & \frac{\Gamma}{g}(m_{\nu-1} d - q_{\nu-1}) \end{pmatrix} G(1, \phi_+) = \sqrt{A} \begin{pmatrix} \frac{m_{\nu+1}}{\Gamma} & \phi_- \frac{\Gamma}{g}(m_\nu d - q_\nu) \\ \frac{m_\nu}{\Gamma} & \phi_- \frac{\Gamma}{g}(m_{\nu-1} d - q_{\nu-1}) \end{pmatrix} G(1, \phi_+) \\ &= \sqrt{A} \begin{pmatrix} \frac{1}{\phi_+} \frac{m_{\nu+1}}{\Gamma} & \phi_+ \phi_- \frac{\Gamma}{g}(m_\nu d - q_\nu) \\ \frac{1}{\phi_+} \frac{m_\nu}{\Gamma} & \phi_+ \phi_- \frac{\Gamma}{g}(m_{\nu-1} d - q_{\nu-1}) \end{pmatrix} \simeq \Omega_\nu(A, \Gamma) \begin{pmatrix} 1 & 0 \\ 0 & -1 \end{pmatrix}. \end{aligned}$$

The last simequality comes from noting that $\phi_+ \phi_- = -1$ and $\frac{m_{\nu+1}}{\phi_+} \simeq m_\nu$. The latter relation is a consequence of the limit $\lim_{\nu \rightarrow \infty} \frac{m_{\nu+1}}{m_\nu} = \phi_+$ which is proven by inspection of Binet's formula while remembering that $|\phi_-|^\nu$ is small for large ν . The convergence is typically (and, in particular for the Fibonacci sequence $m_\nu = f_\nu$) quick, so that we can write $\frac{m_{\nu+1}}{m_\nu} \simeq \phi_+$. This self-similarity is illustrated in Fig. 3, where the lattice points correspond to the maxima of the graphed function. The left column of Fig. 3 illustrates the lattice for $\Gamma = \sqrt{34}$, $\Gamma = \sqrt{34}\phi_+$, and $\Gamma = \sqrt{34}\phi_+^2$, and the right column illustrates the lattice for $\Gamma \simeq 7.52$, $\Gamma \simeq 7.52\phi_+$, and $\Gamma \simeq 7.52\phi_+^2$. (These choices for Γ are motivated by the discussion of rhombic lattices in Section 2.5.)

2.4 Rational Approximations of Noble Numbers

In the classical theory of continued fraction expansions of real numbers, the numbers $(q_0 + q_1\phi_+)/ (m_0 + m_1\phi_+)$, where the integers q_0, q_1, m_0, m_1 satisfy $q_1 m_0 - q_0 m_1 = \pm 1$, carry the distinguished title *noble numbers*. Atela, *et. al.* [11] study their relation to hyperbolic geometry and the van Iterson diagram (which relates the van Iterson parameter to the divergence angle), and the noble numbers and their special continued fraction expansions appear in numerous studies of phyllotaxis [13]. In this section, we will follow some classical theorems on continued fraction expansions and make use of the self-similarity results derived in Section 2.3 to find a limit of quantities that will prove useful in Sections 3 and 4.

We begin with a brief overview of continued fraction expansions with reference to theorems proved in Hardy and Wright [10]. Any $\xi \in \mathbb{R}$ has a unique continued fraction expansion

$$\xi = a_0 + \frac{1}{a_1 + \frac{1}{a_2 + \frac{1}{a_3 + \cdots + \frac{1}{a_n + \cdots}}}}$$

where $a_0 \in \mathbb{Z}$ and $a_i \in \mathbb{N}$ for $i \geq 1$. The right-hand side is more compactly written as $\xi = [a_0, a_1, a_2, \dots]$, and the equality means that the sequence

$$\frac{p_\nu}{z_\nu} = [a_0, a_1, \dots, a_\nu, 0, 0, \dots] \doteq [a_0, a_1, \dots, a_\nu]$$

of rational numbers converges to ξ . Now suppose that $\xi \in \mathbb{R} - \mathbb{Q}$. The number $\frac{p_\nu}{z_\nu}$, called the ν th *convergent* to ξ , is the best rational approximation of ξ in that if $n > 1$, $0 < z < z_\nu$, and $\frac{p}{z} \neq \frac{p_\nu}{z_\nu}$, then

$$\left| \frac{p_\nu}{z_\nu} - \xi \right| < \left| \frac{p}{z} - \xi \right|$$

([10], Theorem 181). Furthermore, the quality of the approximation $\frac{p_\nu}{z_\nu}$ is estimated in terms of z_ν and $a_{\nu+1}$ by the inequality

$$\left| \frac{p_\nu}{z_\nu} - \xi \right| < \frac{1}{z_\nu^2 a_{\nu+1}} \quad (3)$$

([10], page 163). An irrational number ξ can thus be approximated by rationals best if the integers a_ν are large.

Two numbers $\xi, \eta \in \mathbb{R}$ are said to be *equivalent* if the continued fraction expansion for ξ after some term a_μ is the same as the expansion of η after some term b_ν ; *i.e.*,

$$\xi = [a_0, a_1, \dots, a_\mu, c_0, c_1, \dots], \quad \eta = [b_0, b_1, b_2, \dots, b_\nu, c_0, c_1, \dots].$$

This condition is an equivalence relation on \mathbb{R} and can be expressed as

$$\xi = \frac{q_0 + q_1 \eta}{m_0 + m_1 \eta}$$

for integers q_i, m_i such that $q_1 m_0 - q_0 m_1 = \pm 1$ ([10], Theorem 73). The number ϕ_+ has the continued fraction expansion $\phi_+ = [1, 1, 1, \dots]$, and the numbers $(q_0 + q_1 \phi_+) / (m_0 + m_1 \phi_+)$ (with $q_0 m_1 - m_0 q_1 = \pm 1$) in its equivalence class are in the sense of (3) the most difficult irrational numbers to approximate by rationals. However, an infinite number of rational approximations will satisfy an inequality which, for ϕ_+ and the members of its equivalence class, is stronger than (3). Any irrational ξ also has an infinite number of rational approximations $\frac{p}{z}$ which satisfy ([10], Theorem 185)

$$\left| \frac{p}{z} - \xi \right| < \frac{1}{z^2 \sqrt{5}}.$$

Rewritten,

$$z|z\xi - p| < \frac{1}{\sqrt{5}}. \quad (4)$$

This is the best possible result in that $\sqrt{5}$ can not be replaced by any larger number. Specifically, Hardy and Wright show that for $\xi = \phi_+$, the assumption that an infinite number of rationals $\frac{p}{z}$ satisfy an inequality $|\frac{p}{z} - \xi| < \frac{1}{z^2 \eta}$ (that is, $z|z\xi - p| < \frac{1}{\eta}$) for $\eta > \sqrt{5}$ leads to a contradiction. From this we can conclude that there is a sequence of rationals $\frac{p_\nu}{z_\nu}$ such that $z_\nu |z_\nu \phi_+ - p_\nu|$ converges to $\frac{1}{\sqrt{5}}$ from below. A similar conclusion can be reached for any of the noble numbers.

The numbers $\frac{q_\nu}{m_\nu}$ are not, in general, the ν th convergents to $\hat{d}(m_0, m_1, q_0, q_1) = \frac{q_0 + q_1 \phi_+}{m_0 + m_1 \phi_+}$, but using Binet's formula one can show that they do converge to \hat{d} ;

$$\lim_{\nu \rightarrow \infty} \frac{q_\nu}{m_\nu} = \frac{q_0 + q_1 \phi_+}{m_0 + m_1 \phi_+}.$$

Inspired by (4), we calculate the quantities $m_\nu(m_\nu \hat{d} - q_\nu)$ and arrive at

Proposition 2: Given two Fibonacci-like sequences q_ν and m_ν , respectively generated by q_0, q_1 and m_0, m_1 , define $g = q_1 m_0 - q_0 m_1$ and $\hat{d} = \frac{q_0 + q_1 \phi_+}{m_0 + m_1 \phi_+}$. Then,

$$\lim_{k \rightarrow \infty} \frac{m_{2k}}{g} (m_{2k} \hat{d} - q_{2k}) = \frac{1}{\sqrt{5}},$$

and

$$\lim_{k \rightarrow \infty} \frac{m_{2k+1}}{g} (m_{2k+1} \hat{d} - q_{2k+1}) = -\frac{1}{\sqrt{5}}.$$

Proof 1: Using Binet's formula to express m_ν, q_ν in terms of m_0, m_1, q_0, q_1 , write

$$\frac{m_\nu}{q_1 m_0 - q_0 m_1} \left(m_\nu \frac{q_0 + q_1 \phi_+}{m_0 + m_1 \phi_+} - q_\nu \right) = \frac{(-1)^\nu (m_0 + m_1 \phi_+) + \phi_-^{2\nu-2} (m_0 + m_1 \phi_-)}{\sqrt{5} (m_0 + m_1 \phi_+)}.$$

Now note that $|\phi_-| < 1$. ■

A second proof makes use of the ν -invariant nature of g and \hat{d} .

Proof 2:

$$\begin{aligned} & \frac{m_\nu}{q_1 m_0 - q_0 m_1} \left(m_\nu \frac{q_0 + q_1 \phi_+}{m_0 + m_1 \phi_+} - q_\nu \right) = (-1)^\nu \frac{m_\nu}{q_{\nu+1} m_\nu - q_\nu m_{\nu+1}} \left(m_\nu \frac{q_\nu + q_{\nu+1} \phi_+}{m_\nu + m_{\nu+1} \phi_+} - q_\nu \right) \\ & = (-1)^\nu \frac{m_\nu}{q_{\nu+1} m_\nu - q_\nu m_{\nu+1}} \left(\frac{(q_{\nu+1} m_\nu - q_\nu m_{\nu+1}) \phi_+}{m_\nu + m_{\nu+1} \phi_+} \right) = \frac{m_\nu \phi_+}{m_\nu + m_{\nu+1} \phi_+} = (-1)^\nu \frac{\phi_+}{1 + \frac{m_{\nu+1}}{m_\nu} \phi_+}. \end{aligned}$$

The limit $\lim_{\nu \rightarrow \infty} \frac{m_{\nu+1}}{m_\nu} = \phi_+$ and equalities $|\phi_-| = \frac{1}{\phi_+} = 1 + \phi_+^2$ and $|\phi_-| + \phi_+ = \sqrt{5}$ complete the proof. \blacksquare

Note also that for $d \neq \hat{d}(m_0, m_1, q_0, q_1)$, the sequence $|\frac{m_\nu}{g}(m_\nu d - q_\nu)|$ diverges. Proposition 2 holds for any $q_0, q_1, m_0, m_1 \in \mathbb{R}$, but in the context of cylindrical lattices, we take $m_0, m_1 \in \mathbb{N}$ and choose $q_0, q_1 \in \mathbb{Z}$ such that $q_1 m_0 - q_0 m_1 = \gcd(m_0, m_1) = g$.

For the classical Fibonacci sequence, it is convenient to take $m_0 = 0, m_1 = 1$. Then, $\gcd(m_0, m_1)$ is not defined, but for $q_0 = -1, q_1 = 1, q_0 m_1 - q_1 m_0 = 1$, and $q_\nu m_{\nu+1} - q_{\nu+1} m_\nu = (-1)^\nu = (-1)^\nu \gcd(m_\nu, m_{\nu+1})$ for $\nu \geq 1$. Writing f_ν for the ν th (classical) Fibonacci number, $m_\nu = f_\nu$ and $q_\nu = f_{\nu-1}$. Proposition 2 tells us to consider the special value $d = (-1 + \phi_+)/ (0 + \phi_+) = 1 + \phi_-$ and gives us the limit

$$\lim_{\nu \rightarrow \infty} f_\nu |f_\nu (1 + \phi_-) - f_{\nu-2}| = \frac{1}{\sqrt{5}}.$$

Consider now the matrix $\hat{\Omega}_\nu$ in light of Proposition 2. Defining $\rho_\nu \doteq \frac{\Gamma}{m_\nu}$,

$$\hat{\Omega}_\nu(A, \Gamma) = \sqrt{A} \begin{pmatrix} \frac{1}{\rho_\nu} & \rho_\nu \frac{1}{g} m_\nu (m_\nu \hat{d} - q_\nu) \\ \frac{1}{\rho_{\nu-1}} & \rho_{\nu-1} \frac{1}{g} m_{\nu-1} (m_{\nu-1} \hat{d} - q_{\nu-1}) \end{pmatrix} \simeq \sqrt{A} \begin{pmatrix} \frac{1}{\rho_\nu} & \rho_\nu \frac{\pm 1}{\sqrt{5}} \\ \frac{1}{\rho_{\nu-1}} & \rho_{\nu-1} \frac{\mp 1}{\sqrt{5}} \end{pmatrix}.$$

This tells us that the sequence $\vec{\omega}_\nu$ of basis vectors lies near the curves $\sqrt{A} \left(\frac{1}{\rho}, \pm \frac{\rho}{\sqrt{5}} \right)$ parametrized by ρ . These curves are illustrated in Fig. 3.

2.5 Rhombic Cylindrical Lattices

So far, we have taken d to be a constant. The divergence angle in real plants does vary throughout the pattern, and often considerably. van Iterson [30] (see also [5]) showed how d can be chosen as a function of a parameter analogous to Γ , so that, as Γ increases continuously, the lattice $\mathbb{L}(A, \Gamma, d, g)$ is always *rhombic*. That is, for a vector sequence $\vec{\omega}_\nu$ and a sequence Γ_ν , $\|\vec{\omega}_\nu\| = \|\vec{\omega}_{\nu+1}\|$ for $\Gamma_\nu \leq \Gamma \leq \Gamma_{\nu+1}$. The values $\Gamma_\nu^2 = \frac{2}{\sqrt{3}}(m_\nu^2 + m_\nu + m_{\nu+1} + m_{\nu+1}^2)$, $d = \frac{m_{\nu+1} q_\nu + m_\nu q_{\nu+1} + 2(m_{\nu+1} q_{\nu+1} + m_\nu q_\nu)}{2(m_\nu^2 + m_\nu m_{\nu+1} + m_{\nu+1}^2)}$ are found by solving the equation $\|\vec{\omega}_\nu\| = \|\vec{\omega}_{\nu+1}\| = \|\vec{\omega}_{\nu+2}\|$ for Γ and d .

The choices of d and Γ that yield orthogonal lattices—lattices for which $\vec{\omega}_\nu$ and $\vec{\omega}_{\nu+1}$ have the same length and are orthogonal to each other—are found by solving $\Omega_{\nu+1}^T \Omega_{\nu+1} = AI$, where I is the identity matrix. From

$$\Omega_{\nu+1}^T \Omega_{\nu+1} = A \begin{pmatrix} \frac{m_\nu^2 + m_{\nu+1}^2}{\Gamma^2} & \frac{m_\nu}{g} (m_\nu d - q_\nu) + \frac{m_{\nu+1}}{g} (m_{\nu+1} d - q_{\nu+1}) \\ \frac{m_\nu}{g} (m_\nu d - q_\nu) + \frac{m_{\nu+1}}{g} (m_{\nu+1} d - q_{\nu+1}) & \frac{\Gamma^2}{g^2} [(m_\nu d - q_\nu)^2 + (m_{\nu+1} d - q_{\nu+1})^2] \end{pmatrix} = AI,$$

one immediately sees that $\Gamma^2 = m_\nu^2 + m_{\nu+1}^2$ and, completing the calculation, one arrives at $d = \frac{q_\nu m_\nu + q_{\nu+1} m_{\nu+1}}{m_\nu^2 + m_{\nu+1}^2}$. To relate this to Proposition 2, we note that

$$\lim_{\nu \rightarrow \infty} \frac{m_\nu}{g} \left| m_\nu \frac{q_\nu m_\nu + q_{\nu+1} m_{\nu+1}}{m_\nu^2 + m_{\nu+1}^2} - q_\nu \right| = \lim_{\nu \rightarrow \infty} \frac{m_\nu m_{\nu+1}}{m_\nu^2 + m_{\nu+1}^2} = \frac{1}{\sqrt{5}}.$$

In the following, we write $\Gamma_{\nu, H}^2 = \frac{2}{\sqrt{3}}(m_\nu^2 + m_\nu + m_{\nu+1} + m_{\nu+1}^2)$ (H for *hexagon*), and $\Gamma_{\nu, S}^2 = m_\nu^2 + m_{\nu+1}^2$ (S for *square*).

3 Functions with Lattice Periodicity

In the previous section, we described patterns in terms of lattices and Voronoi tiles. Actual plant surfaces are, however, three-dimensional structures—deformations of a disk or sphere into surfaces with peaks and valleys. The peaks correspond to the centers of the phylla and give the lattice points; the valleys trace out the tiles. In this section, we describe plant surfaces in terms of functions $w(s, \theta)$ that are periodic with respect to a cylindrical lattice \mathbb{L} . Voronoi mountain functions and length-amplitude functions are introduced in Sections 3.2 and 3.3 as examples of \mathbb{L} -periodic functions.

3.1 The Dual Lattice

Given a lattice $\mathbb{L} = \{z_1\vec{v} + z_2\vec{w} : (z_1, z_2) \in \mathbb{Z}^2\}$, a function $w(\vec{x})$ is \mathbb{L} -periodic if $w(\vec{x} + \vec{\omega}) = w(\vec{x})$ for all $\vec{x} \in \mathbb{R}^2$, $\vec{\omega} \in \mathbb{L}$, or, equivalently, if for all $\vec{x} \in \mathbb{R}^2$

$$w(\vec{x} + \vec{v}) = w(\vec{x} + \vec{w}) = w(\vec{x}).$$

Denoting the space of smooth real-valued \mathbb{L} -periodic functions by $C_{\mathbb{L}}^{\infty}(\mathbb{R}^2, \mathbb{R})$, any $w \in C_{\mathbb{L}}^{\infty}(\mathbb{R}^2, \mathbb{R})$ has a Fourier series expansion

$$w(\vec{x}) = \sum_{(z_1, z_2) \in \mathbb{Z}^2} A_{(z_1, z_2)} e^{i(z_1\vec{k}_m + z_2\vec{k}_n) \cdot \vec{x}}, \quad A_{(-z_1, -z_2)} = A_{(z_1, z_2)}^* \quad (5)$$

for complex amplitudes $A_{(z_1, z_2)}$. The condition $A_{(-z_1, -z_2)} = A_{(z_1, z_2)}^*$, where $*$ denotes the complex conjugate, insures that w is real-valued. The vectors \vec{k}_m, \vec{k}_n are a basis for the dual lattice \mathbb{K} to \mathbb{L} . For a cylindrical lattice $\mathbb{L}(A, \Gamma, d, g)$ with basis matrix

$$\Omega_{(m, n)}(A, \Gamma, d, g) = \sqrt{A} \begin{pmatrix} \frac{n}{\Gamma} & \frac{\Gamma}{g}(nd - p) \\ \frac{m}{\Gamma} & \frac{\Gamma}{g}(md - q) \end{pmatrix},$$

the dual vectors \vec{k}_m, \vec{k}_n are given by

$$\begin{pmatrix} -\vec{k}_m^t & \vec{k}_n^t \end{pmatrix} = K = 2\pi\Omega^{-1} = \frac{2\pi}{\sqrt{A}} \begin{pmatrix} -\frac{\Gamma}{g}(q - md) & \frac{\Gamma}{g}(p - nd) \\ -\frac{m}{\Gamma} & \frac{n}{\Gamma} \end{pmatrix}.$$

That is,

$$\vec{k}_m = \frac{2\pi}{\sqrt{A}} \left(\frac{\Gamma}{g}(q - md), \frac{m}{\Gamma} \right), \quad \vec{k}_n = \frac{2\pi}{\sqrt{A}} \left(\frac{\Gamma}{g}(p - nd), \frac{n}{\Gamma} \right).$$

The sequence Ω_{ν} of basis vectors gives rise to a sequence of dual basis vectors

$$K_{\nu} = 2\pi\Omega_{\nu}^{-1} = \frac{2\pi}{\sqrt{A}} \begin{pmatrix} -\frac{\Gamma}{g}(q_{\nu} - m_{\nu}d) & \frac{\Gamma}{g}(q_{\nu+1} - m_{\nu+1}d) \\ -\frac{m_{\nu}}{\Gamma} & \frac{m_{\nu+1}}{\Gamma} \end{pmatrix},$$

and associated sequences of dual vectors

$$\vec{k}_{\nu} = \frac{2\pi}{\sqrt{A}} \left(\frac{\Gamma}{g}(q_{\nu} - m_{\nu}d), \frac{m_{\nu}}{\Gamma} \right). \quad (6)$$

In analogy to $\hat{\Omega}(A, \Gamma)$, we define

$$\hat{K}_{\nu}(A, \Gamma) = K_{\nu}(A, \Gamma, d = \hat{d}).$$

Then, for $\rho_{\nu} = \frac{\Gamma}{m_{\nu}}$,

$$\hat{K}_{\nu}(A, \Gamma) = \frac{2\pi}{\sqrt{A}} \begin{pmatrix} -\rho_{\nu} \frac{m_{\nu}}{g}(q_{\nu} - m_{\nu}\hat{d}) & \rho_{\nu+1} \frac{m_{\nu+1}}{g}(q_{\nu+1} - m_{\nu+1}\hat{d}) \\ -\frac{1}{\rho_{\nu}} & \frac{1}{\rho_{\nu+1}} \end{pmatrix} \simeq \frac{2\pi}{\sqrt{A}} \begin{pmatrix} -\rho_{\nu} \left(\mp \frac{1}{\sqrt{5}} \right) & \rho_{\nu+1} \left(\pm \frac{1}{\sqrt{5}} \right) \\ -\frac{1}{\rho_{\nu}} & \frac{1}{\rho_{\nu+1}} \end{pmatrix}.$$

The dual basis vectors lie close to the curves $\left(\pm \frac{\rho}{\sqrt{5}}, \frac{1}{\rho} \right)$ illustrated in Fig. 4.

3.2 Voronoi Mountain Surfaces

Given a set of points P in the (s, θ) -plane, a Voronoi mountain function V_P is defined by

$$V_P(s, \theta) = -\text{distance}((s, \theta), P(s, \theta)).$$

That is, $V_P(s, \theta)$ is the negative distance of (s, θ) to the closest point in P . For $P = \mathbb{L}$, $V_P(s, \theta) = V_{\mathbb{L}}(s, \theta)$ is an \mathbb{L} -periodic function. In Fig. 3 are illustrated the Voronoi mountain functions $V_{\mathbb{L}}$ for $\mathbb{L} = \mathbb{L}(A = 1, \Gamma, d = 1 + \phi_-, g = 1)$, and increasing values of $\Gamma = \Gamma_{4,S}, \Gamma_{4,H}, \Gamma_{5,S}, \Gamma_{5,H}, \Gamma_{6,S}, \Gamma_{6,H}$, where $m_0 = 0, m_1 = 1$, so that $\Gamma_{4,S}$ corresponds to $m_4 = 3$, $\Gamma_{5,S}$ to $m_5 = 5$, and $\Gamma_{6,S}$ to $m_6 = 8$. Note that we use $d = 1 + \phi_-$ for each graph, not the values of d computed in Section 1.5 that give an exact square or hexagonal lattice. $V_{\mathbb{L}}$ is illustrated on the right half of each graph. The left half of each graph is a smooth approximation of $V_{\mathbb{L}}$, constructed as follows: The Fourier transforms of the functions $V_{\mathbb{L}}$, computed in MATLAB, are illustrated in Fig. 4. These plots give the amplitudes $A_{\vec{k}}$ associated to vectors \vec{k} in the wavevector space, and one notices peaks which lie near the curves $(\pm \frac{\rho}{\sqrt{5}}, \frac{1}{\rho})$ computed in Section 2.1. The Voronoi mountain functions are approximated by

$$V_{\mathbb{L}}(s, \theta) \simeq \sum A_{\nu} \cos(\vec{k}_{\nu} \cdot (s, \theta)),$$

where the sum is taken over members of the wavevector sequence (6). Here, the amplitudes A_{ν} are real, and the terms $A_{\nu} \cos(\vec{k}_{\nu} \cdot (s, \theta))$ (which we will refer to as *modes*) correspond to sums of terms $A_{(z_1, z_2)} e^{i(z_1 \vec{k}_m + z_2 \vec{k}_n) \cdot \vec{x}} + A_{(z_1, z_2)}^* e^{-i(z_1 \vec{k}_m + z_2 \vec{k}_n) \cdot \vec{x}}$ in (5) for $A_{(z_1, z_2)} \in \mathbb{R}$. The Fourier transform indicates that at $\Gamma = \Gamma_{\nu, H}$, $V_{\mathbb{L}}$ is well approximated by one *triad* of modes, meaning a set of three modes with wavevectors $\vec{k}_{\nu}, \vec{k}_{\nu+1}, \vec{k}_{\nu+2} = \vec{k}_{\nu} + \vec{k}_{\nu+1}$. Transitions between triads take place at $\Gamma = \Gamma_{\nu, S}$, where two triads with wavevectors $\vec{k}_{\nu}, \vec{k}_{\nu+1}, \vec{k}_{\nu+2}$ and $\vec{k}_{\nu+1}, \vec{k}_{\nu+2}, \vec{k}_{\nu+3}$ have significant amplitudes as indicated by the Fourier transform. At $\Gamma_{\nu, S}$, the amplitudes are such that $A_{\nu} \simeq A_{\nu+3} \ll A_{\nu+1} \simeq A_{\nu+2}$. As Γ increases, any A_{ν} increases to a maximum value when $|\vec{\omega}_{\nu}|$ is of shortest length, and then decreases. To be able to analytically study amplitudes A_{ν} with this behavior and not have to resort to numerical computation, we define amplitudes \mathcal{A}_{ν} which are simply the inverses of the vector lengths;

$$\mathcal{A}_{\nu} \doteq \frac{A}{|\vec{\omega}_{\nu}|^2} = \frac{1}{\frac{1}{\Gamma^2} m_{\nu}^2 + \frac{\Gamma^2}{g^2} (m_{\nu} d - q_{\nu})^2}.$$

As with Ω_{ν} , the \mathcal{A}_{ν} are considered in the context of given sequences m_{ν}, q_{ν} , and we will write $\hat{\mathcal{A}}_{\nu}$ for \mathcal{A}_{ν} evaluated at $d = \hat{d}(m_0, m_1, q_0, q_1)$. The functions

$$w(s, \theta) = \sum \hat{\mathcal{A}}_{\nu} \cos(\vec{k}_{\nu} \cdot (s, \theta)), \quad (7)$$

where the sum is taken over the three (for $\Gamma = \Gamma_{\nu, H}$) or four (for $\Gamma = \Gamma_{\nu, S}$) modes with largest amplitudes as read off the Fourier transforms, are depicted on the left sides of the plots in Fig. 3 and provide very good approximations to the functions $V_{\mathbb{L}}$. For fixed sequences m_{ν}, q_{ν} , $\hat{\mathcal{A}}_{\nu}$ becomes a function $\hat{\mathcal{A}}_{\nu}(\Gamma)$ of Γ .

The sequence of functions $\hat{\mathcal{A}}_{\nu}(\Gamma)$ associated to the Fibonacci sequence $m_0 = 0, m_1 = 1$ and $d = 1 + \phi_-$ is plotted in Fig. 5. The values $\Gamma_{\nu, S}$ and $\Gamma_{\nu, H}$ are marked as well. One notices that at $\Gamma = \Gamma_{\nu, S}$, $\hat{\mathcal{A}}_{\nu-n} \simeq \hat{\mathcal{A}}_{\nu+n+1}$ for $n = 0, 1, 2, \dots$. This is a consequence of the near-orthogonality of the vectors $\vec{\omega}_{\nu}$; the values $d = \frac{q_{\nu} m_{\nu} + q_{\nu+1} m_{\nu+1}}{m_{\nu}^2 + m_{\nu+1}^2}$ that give orthogonal lattices at $\Gamma_{\nu, S}$ converge very quickly to $d = 1 + \phi_-$. The values $\Gamma_{\nu, H}$ are located near the maxima of the functions $\hat{\mathcal{A}}_{\nu}(\Gamma)$. We will come back to this observation in Section 3.4.

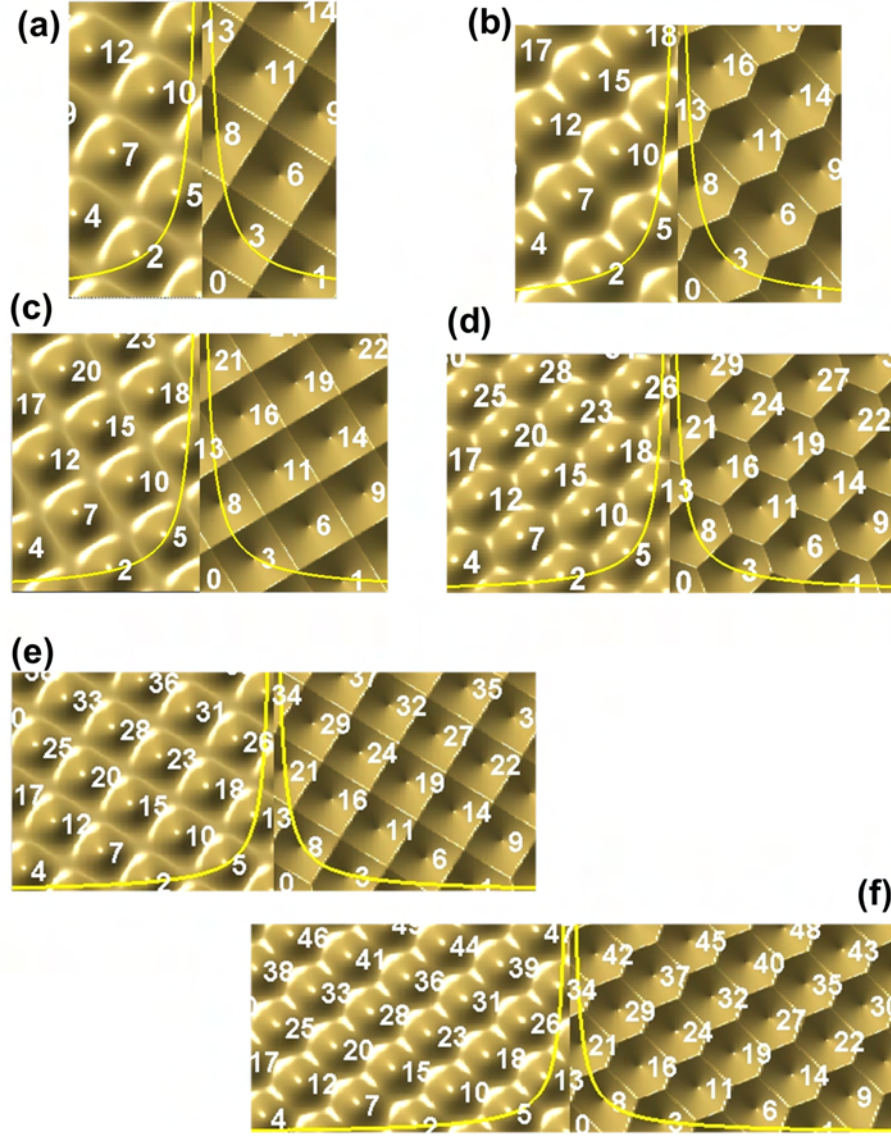


Figure 3: Graphs of \mathbb{L} -periodic functions corresponding to cylindrical lattices $\mathbb{L}(A = 1, \Gamma, d = 1 + \phi_-, g = 1)$, for increasing values of Γ . The horizontal axis is θ , given for the interval $\theta \in [-\Gamma\pi, \Gamma\pi]$, and the vertical axis is s . The right half of each graph is the Voronoi mountain function, and the left half is the Fourier series approximation (7). The values of Γ are, for $m_0 = 0, m_1 = 1$, so that $\nu = 4, 5, 6$ correspond to $m_4 = 3, m_5 = 5, m_6 = 8$, (a) $\Gamma_{4,S} = \sqrt{34}$, (b) $\Gamma_{2,H} \simeq 7.52$, (c) $\Gamma_{5,S} = \sqrt{89}$, (d) $\Gamma_{5,H} \simeq 7.52\phi_+$, (e) $\Gamma_{6,S} = \sqrt{233}$, (f) $\Gamma_{6,H} \simeq 7.52\phi_+^2$. The maxima of the graphs correspond to the points in the lattice \mathbb{L} , and the points are numbered from smallest to largest s -coordinate value. Also plotted on each graph are the curves $\sqrt{A} \left(\frac{1}{\rho}, \pm \frac{\rho}{\sqrt{5}} \right)$ calculated in Section 2.4.

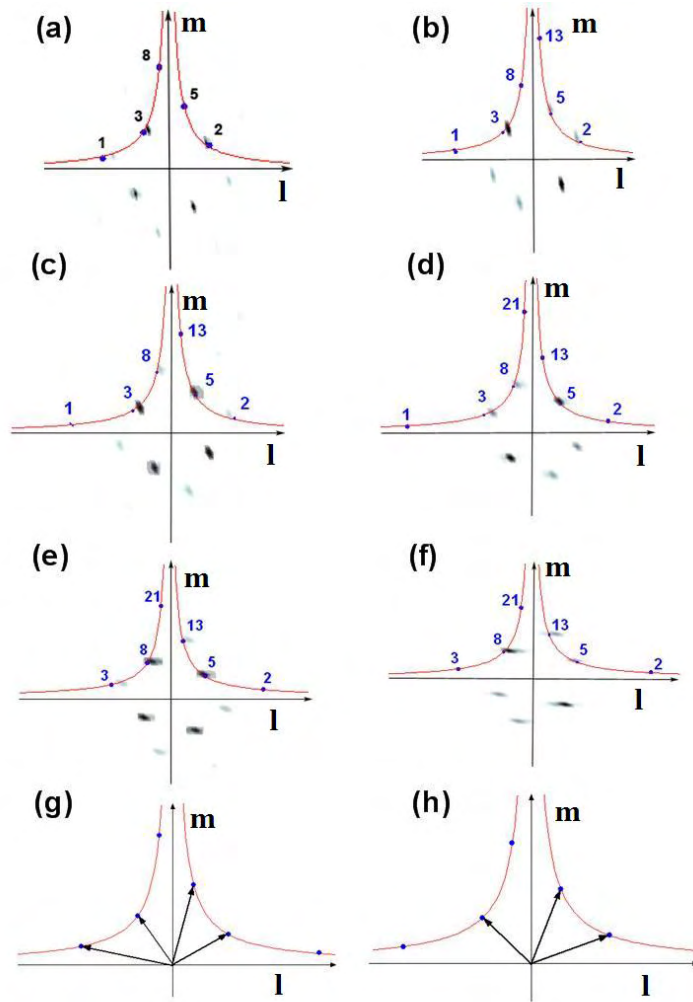


Figure 4: Fourier transforms, computed in MATLAB, of the Voronoi mountain functions graphed in Fig. 3, with (a-f) corresponding to the same respective letters in that figure. The horizontal axis gives the radial wavenumber l and the vertical axis the angular wavenumber m of the Fourier wavevector $\vec{k} = (l, m)$. In (g,h), the typical wavenectors for the $\Gamma_{\nu,S}$ (left column) or $\Gamma_{\nu,H}$ (right column) cases are plotted as vectors. Also displayed are the curves $\left(\pm \frac{\rho}{\sqrt{5}}, \frac{1}{\rho}\right)$ computed in Section 3.1.

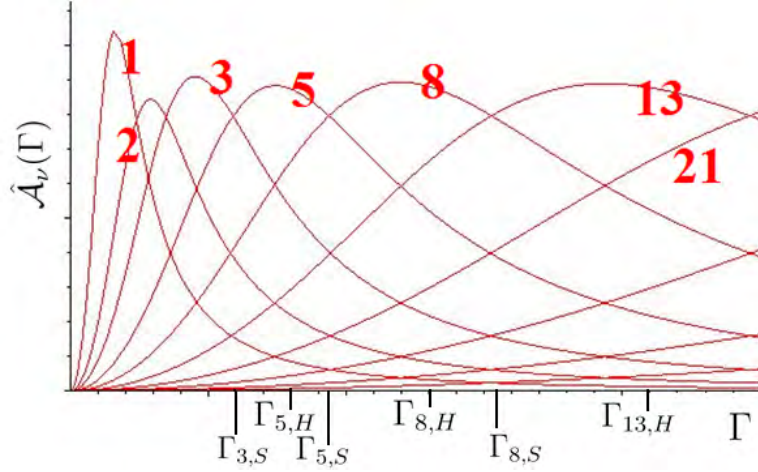


Figure 5: The functions $\hat{\mathcal{A}}_\nu(\Gamma)$ for the sequence generated by $m_0 = 0$, $m_1 = 1$. Each curve is labelled by the corresponding m_ν in the sequence.

3.3 Voronoi Mountain Surfaces on the Annulus

We now translate the ideas from Section 3.2 to the annulus. The Voronoi mountain functions V_P , where P is the set of points in Fig. 2 (b) (that is, the image under T of the lattice $\mathbb{L}(A = 1, \Gamma = 1, d = 1 + \phi_-, g)$), appear in Fig. 6 (b). To approximate V_P with a function analogous to (7), we note that for a cylindrical lattice \mathbb{L} with dual lattice $\mathbb{K} = \{z_1 \vec{k}_m + z_2 \vec{k}_n : (z_1, z_2) \in \mathbb{Z}\}$, the maxima of

$$w(r, \alpha) = \sum_{\vec{k} \in \mathbb{K}} A_{\vec{k}} \cos(\vec{k} \cdot (r^2, \alpha))$$

lie at the points (r^2, α) in \mathbb{L} for positive $A_{\vec{k}}$. In other words, the maxima are at the points $(r, \alpha) = T(r^2, \alpha) \in \{T(\vec{\omega}) : \vec{\omega} \in \mathbb{L}\}$. In Fig. 6 (b) appear the graphs of the functions

$$w(r, \alpha) = \sum \hat{\mathcal{A}}(\Gamma = r) \cos(\vec{k}_\nu \cdot (r^2, \alpha)), \quad (8)$$

where the sum is taken, at any value of r , over the three modes with wavevectors in the sequence $\vec{k}_\nu = \frac{2\pi}{\sqrt{A}} \left(\frac{\Gamma}{g}(q_\nu - m_\nu d), \frac{m_\nu}{\Gamma} \right)$ for $m_0 = 0, m_1 = 1, q_0 = -1, q_0 = 1$ and with largest amplitudes $\hat{\mathcal{A}}_\nu(\Gamma = r)$. The parameter Γ is taken to be $\Gamma = 1$. The quantities $\vec{k}_\nu \cdot (r^2, \alpha)$ can thus be thought of as $\vec{k}_\nu(r) \cdot (r, r\alpha)$, where

$$\vec{k}_\nu(r) = \frac{2\pi}{\sqrt{A}} \left(\frac{r}{g}(q_\nu - m_\nu d), \frac{m_\nu}{r} \right). \quad (9)$$

The coordinate r represents in this way the parameter Γ , and graphs of $w(r, \alpha)$ allow one to see the evolution of the pattern over continuously changing Γ .

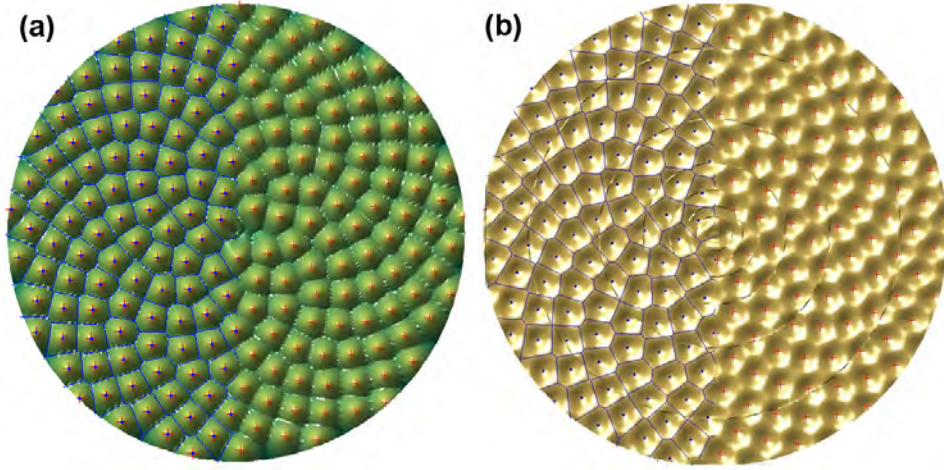


Figure 6: (a) The Voronoi mountain function corresponding to the set of points in Fig. 2(b). (b) The Fourier approximation of the function in (a) given by the r -dependent Fourier series (8). The exact Voronoi polygons are plotted over the left-hand halves of both graphs.

The Voronoi cells and Voronoi mountain surface, while having a certain consistency in shape, do not compare to the regular tilings observed on (idealized) sunflowers or other plants. Symmetries and invariances of the functions $\hat{\mathcal{A}}_\nu(\Gamma)$, discussed in Section 3.4, will lead us to multiple triad surfaces and regular tilings in Section 3.5.

3.4 Invariant Curves

For $\rho_\nu = \frac{2\pi\Gamma}{m_\nu}$,

$$\hat{\mathcal{A}}_\nu(\Gamma) = \frac{1}{\frac{1}{\Gamma^2}m_\nu^2 + \frac{\Gamma^2}{g^2}(m_\nu\hat{d} - q_\nu)^2} = \frac{1}{\frac{1}{\rho_\nu^2} + \rho_\nu^2 \frac{m_\nu^2}{g^2}(m_\nu\hat{d} - q_\nu)^2} \simeq \frac{\rho_\nu^2}{1 + \frac{1}{5}\rho_\nu^4}.$$

The function $\hat{\mathcal{A}}(\rho) = \frac{\rho^2}{1 + \frac{1}{5}\rho^4}$ is plotted in Fig. 7 (a,b,c). The values $\hat{\mathcal{A}}_\nu(\Gamma) = \hat{\mathcal{A}}\left(\frac{\Gamma}{m_\nu}\right)$ for $m_\nu = f_\nu$ in the Fibonacci sequence are represented as marked points on the graphs, and as Γ increases, the points flow to the right along the curve. The maximum value of $\hat{\mathcal{A}}(\rho)$ is $\hat{\mathcal{A}}(\sqrt[4]{5}) = \frac{\sqrt{5}}{2}$, and for any $\mu \in \mathbb{R}$, $\hat{\mathcal{A}}(\mu\sqrt[4]{5}) = \hat{\mathcal{A}}\left(\frac{1}{\mu}\sqrt[4]{5}\right) = \sqrt{5}\frac{1}{\mu^2 + \frac{1}{\mu^2}}$. We now exploit this symmetry in $\hat{\mathcal{A}}$ in examining the special values $\Gamma \in \{\Gamma_{\nu,S}\}$ and $\Gamma \in \{\Gamma_{\nu,H}\}$. It will be useful to keep in mind the approximation $m_\nu\phi_+^n \simeq m_{\nu+n}$ for $n \in \mathbb{Z}$ (which comes from inspection of Binet's formula).

For $\Gamma = \Gamma_{\nu,S} = \sqrt{m_\nu^2 + m_{\nu+1}^2}$, $\frac{\Gamma^2}{m_\nu^2} = 1 + \frac{m_{\nu+1}^2}{m_\nu^2} \simeq 1 + \phi_+^2 = \phi_+ + \sqrt{5}$, so that $\frac{\Gamma}{m_\nu} \simeq \sqrt{\phi_+}\sqrt[4]{5}$. Then, for $n \in \mathbb{N}$, $\hat{\mathcal{A}}\left(\frac{\Gamma}{m_{\nu-n}}\right) \simeq \hat{\mathcal{A}}\left(\phi_+^n \frac{\Gamma}{m_\nu}\right) = \hat{\mathcal{A}}(\phi_+^n \sqrt{\phi_+}\sqrt[4]{5}) = \hat{\mathcal{A}}\left(\frac{\phi_+^{n+1}}{\sqrt{\phi_+}}\sqrt[4]{5}\right) = \hat{\mathcal{A}}\left(\frac{1}{\phi_+^{n+1}}\sqrt{\phi_+}\sqrt[4]{5}\right) = \hat{\mathcal{A}}\left(\frac{1}{\phi_+^{n+1}}\frac{\Gamma}{m_\nu}\right) \simeq \hat{\mathcal{A}}\left(\frac{\Gamma}{m_{\nu+n+1}}\right)$. In summary,

$$\hat{\mathcal{A}}_{\nu-n}(\Gamma_{\nu,S}) = \hat{\mathcal{A}}\left(\frac{\Gamma_{\nu,S}}{m_{\nu-n}}\right) \simeq \hat{\mathcal{A}}\left(\frac{\Gamma_{\nu,S}}{m_{\nu+n+1}}\right) = \hat{\mathcal{A}}_{\nu+n+1}(\Gamma_{\nu,S}). \quad (10)$$

Recall the assertion in Section 3.2 that the maxima of the functions $\hat{\mathcal{A}}_{\nu+1}(\Gamma)$ occur near $\Gamma = \Gamma_{\nu,H}$. To calculate this, we use that the maximum of $\hat{\mathcal{A}}_{\nu+1}(\Gamma) = \hat{\mathcal{A}}\left(\frac{\Gamma}{m_{\nu+1}}\right)$ occurs at $\frac{\Gamma}{m_{\nu+1}} = \sqrt[4]{5}$, or $\Gamma = \sqrt[4]{5}m_{\nu+1}$.

Defining $\Gamma_{\nu+1,M} = \sqrt[4]{5}m_{\nu+1}$, $\frac{\Gamma_{\nu+1,H}^2}{\Gamma_{\nu+1,M}^2} = \frac{2}{\sqrt{15}} \left(\frac{m_\nu^2}{m_{\nu+1}^2 + m_\nu^2} + 1 \right)$, which converges to $\frac{2}{\sqrt{15}}(\phi_-^2 + |\phi_-| + 1) = \frac{4}{\sqrt{15}}$.

Now suppose that $\Gamma = \Gamma_{\nu,M}$, so that $\frac{\Gamma}{m_\nu} = \sqrt[4]{5}$. Then, $\hat{\mathcal{A}}\left(\phi_+^n \frac{\Gamma}{m_\nu}\right) = \hat{\mathcal{A}}\left(\frac{1}{\phi_+^n} \frac{\Gamma}{m_\nu}\right)$, and we conclude that

$$\hat{\mathcal{A}}_{\nu-n}(\Gamma_{\nu,M}) = \hat{\mathcal{A}}\left(\frac{\Gamma_{\nu,M}}{m_{\nu-n}}\right) \simeq \hat{\mathcal{A}}\left(\frac{\Gamma_{\nu,M}}{m_{\nu+n}}\right) = \hat{\mathcal{A}}_{\nu+n}(\Gamma_{\nu,M}). \quad (11)$$

These symmetries can also be observed by writing the function of two variables

$$\hat{\mathcal{A}}(\nu, \Gamma) = \frac{\left(\frac{\Gamma}{m_0 \phi_+^\nu}\right)^2}{1 + \frac{1}{5} \left(\frac{\Gamma}{m_0 \phi_+^\nu}\right)^4}$$

(replacing m_0 by m_1 if $m_0 = 0$). As $m_\nu \simeq m_0 \phi_+^\nu$, $\hat{\mathcal{A}}(\nu, \Gamma) \simeq \hat{\mathcal{A}}\left(\frac{\Gamma}{m_\nu}\right)$. $\hat{\mathcal{A}}(\nu, \Gamma)$ is symmetric about its maximum, which travels to the right as Γ increases; see Fig. 7 (d,e,f). The symmetries (10,11) are observed for $\Gamma = \Gamma_{\nu,S}$ and $\Gamma_{\nu,M}$.

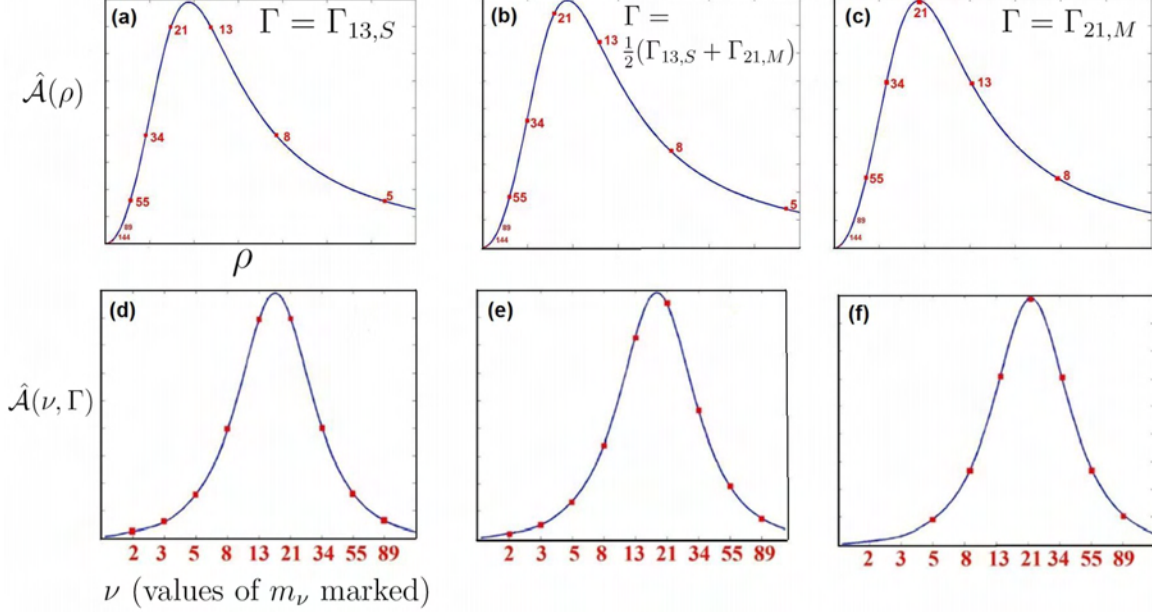


Figure 7: Γ -invariant curves for (a,d) $\Gamma = \Gamma_{13,S}$, (b,e) $\Gamma = \frac{1}{2}(\Gamma_{13,S} + \Gamma_{21,M})$, (c,f) $\Gamma = \Gamma_{21,M}$. Top row: The function $\hat{\mathcal{A}}(\rho)$ with the points $\left(\frac{\Gamma}{m_\nu}, \hat{\mathcal{A}}\left(\frac{\Gamma}{m_\nu}\right)\right)$ marked for m_ν in the Fibonacci sequence. Bottom row: The function $\hat{\mathcal{A}}(\nu, \Gamma)$ is plotted as a function of ν . The horizontal axis is ν , but marked are the integers m_ν for the appropriate values of ν on the axis and m_ν in the Fibonacci sequence.

As a function of ν , $\hat{\mathcal{A}}(\nu, \Gamma)$ is integrable and independent of Γ ;

$$\int_{-\infty}^{\infty} \hat{\mathcal{A}}(\nu, \Gamma) d\nu = \frac{1}{4} \frac{\pi\sqrt{5}}{\ln(\phi_+)} \simeq 3.6495.$$

The infinite sum $\sum_\nu \hat{\mathcal{A}}_\nu(\Gamma)$ is then also nearly constant with respect to Γ , and this is an indication that a sort of Γ -invariance can be achieved by including all terms, not just the three or four with the largest amplitudes, in the Fourier representation of an \mathbb{L} -periodic function.

3.5 Multiple Triad Surfaces

In Fig. 8 (a), we plot the function

$$w(r, \alpha) = \sum_{\nu=1}^{12} \hat{\mathcal{A}}_\nu(r) \cos(\vec{k}_\nu \cdot (r^2, \alpha)), \quad (12)$$

where we have included the first 12 modes with wavevectors in the sequence \vec{k}_ν (that is, the first 10 triads). In this graph, the *shapes*, not only the local lattice, are similar throughout the annulus. However, we must

also observe that the square-shaped tiles of Fig. 8 contrast with the diamond-shaped tiles observed, for example, in sunflowers. But, diamonds are squares under an appropriate choice of metric used to calculate the lengths $\|\vec{\omega}_m\|$. Computed using the metric

$$A^2(A'^2 dr^2 + d\alpha^2),$$

the length-amplitudes become

$$\hat{\mathcal{A}}_{\nu, A'} = \frac{A}{A^2 \left(A'^2 \frac{m_\nu^2}{\Gamma^2} + \frac{\Gamma^2}{g^2} m_\nu^2 (m_\nu \hat{d} - q_\nu)^2 \right)} \simeq \frac{\rho_\nu^2}{A \left(A'^2 + \frac{1}{5} \rho_\nu^4 \right)}.$$

Dependence on A is hidden in $\rho_\nu = \frac{\Gamma}{m_\nu} = \frac{2\pi R}{\sqrt{A m_\nu}}$. Defining $\rho'_\nu = \frac{2\pi R}{m_\nu}$, we have that

$$\frac{\rho_\nu^2}{A \left(A'^2 + \frac{1}{5} \rho_\nu^4 \right)} = \frac{\frac{1}{A} \rho_\nu'^2}{A \left(A'^2 + \frac{1}{5} \frac{1}{A^2} \rho_\nu'^4 \right)} = \frac{\rho_\nu'^2}{A^2 A'^2 + \frac{1}{5} \rho_\nu'^4}.$$

Changing the metric from $A^2(dr^2 + d\alpha^2)$ to $A^2(A'^2 dr^2 + d\alpha^2)$ corresponds to changing the area parameter used in the calculation of $\hat{\mathcal{A}}_\nu$, with the longer axis of the diamonds oriented radially. Diamonds oriented azimuthally correspond to $A' > 1$.

The graph of

$$w(r, \alpha) = \sum_{\nu} \hat{\mathcal{A}}_{\nu, A'}(r) \cos(\vec{k}_\nu \cdot (r^2, \alpha)) \quad (13)$$

for $A' = \frac{1}{2}$ appears in Fig. 8 (b). The wavevectors \vec{k}_ν are exactly the same as those used for Fig. 8 (a), so that the underlying lattices are the same in both figures. The change from A to AA' in the calculation of the amplitudes allows for diamond-shaped tiles.

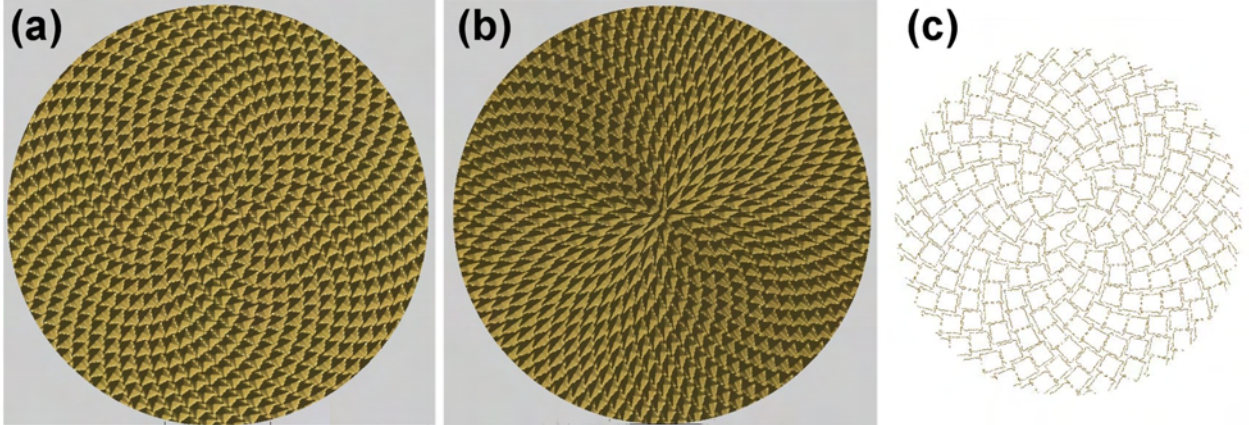


Figure 8: (a) The multi-triad function (12) corresponding to the Fibonacci sequence. (b) The function (13), again corresponding to the Fibonacci sequence, but with $A' = \frac{1}{2}$. (c) A level set of a portion of the graph in (a), showing the outline of diamonds and the gaps between them.

We compare these graphs with the sunflower head of Fig. 9 (a). The sunflower head is not a flat disc (the surface was less curved, but still not flat, when the pattern was formed), so, to facilitate the comparison, we make a cast of a cross section of the head which can be flattened as in Fig. 9 (b). A similar cross section is made of Fig. 8 (b), as shown in Fig. 9 (d,e). While the area of the bracts in the sunflower increase somewhat as the radius increases, similar patterns of diamonds, modulating between offset diamonds and diamonds that meet at four corners, are apparent in both the real sunflower and the theoretical graph.

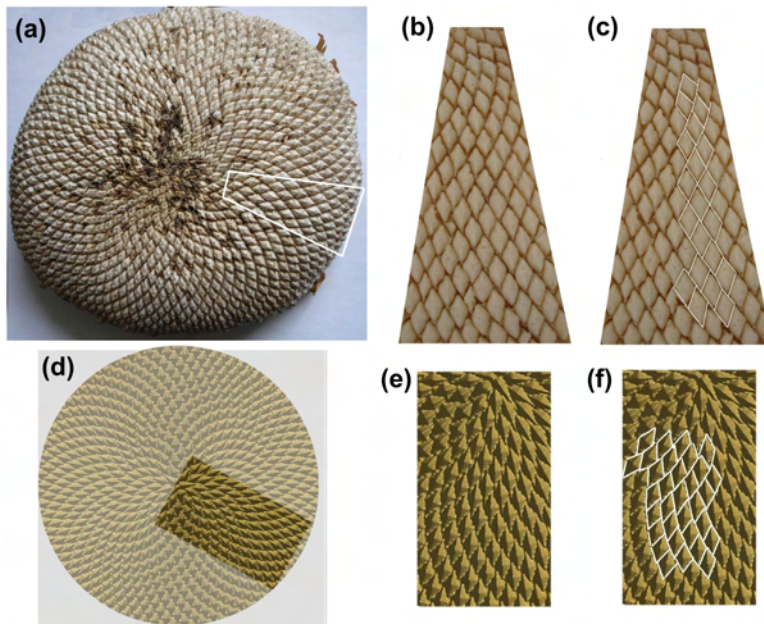


Figure 9: (a) A sunflower seed head and (b,c) a flattened cast of the cross section marked in (a). In (c), outlines of the diamonds are marked; note the evolution of offset diamonds near the top to a pattern of diamonds meeting at four corners, to offset diamonds near the bottom. A similar pattern is seen in a cross section of Fig. 8 (b), as demonstrated in the bottom row.

The polygons observed in Fig. 8 (a,b) are roughly the same throughout the disk, but it is clear that they can not be both true straight-sided polygons and completely tile the disk. To get an idea of how well the disk may be tiled by diamonds, we show in Fig. 8 (c) one contour level of a portion of the graph in Fig. 8 (a), corresponding to a level set near the minimum value of the function. This gives a rough picture of how tiles can be oriented to cover much of the annulus. The question which arises (and is not to be answered here) is what shape and arrangement of tiles can maximally cover the annulus. This extends the idea of maximal packing by disks of a given diameter as described in the introduction.

4 Mechanistic Models and Amplitude Equations

In this section, we briefly describe how the symmetries discussed in the previous sections can play a role in analyzing models for phyllotactic patterns based on the biochemical or biophysical mechanisms responsible for the formation of the patterns in nature. Many different phenomena in nature and in the laboratory give rise to patterns of diamonds, hexagons, or ridges. Examples include Raleigh-Bènard convection experiments, the Rosenzweig instability in ferrofluids [8], and geological formations [15]. In all of these systems, an initially homogeneous state is broken to a state of discrete symmetry as a control parameter crosses a threshold value. The resulting pattern is determined by universal symmetries as well as details of the microscopic mechanism. The latter influence, for example, the winning configuration in the competition between hexagons and ridges and determine the length scale of the pattern. In [17], we show how models that have been proposed for biophysical mechanisms for primordium formation (in which, following the hypothesis of Green [9], primordia arise due to buckling induced by compressive stresses that result from differential growth) and biochemical mechanisms (in particular, the diffusion and transport by PIN1 proteins of the growth hormone auxin, as proposed by Kuhlemeier, *et. al.* [20]) have similar mathematical form and can be analyzed by reduction to similar sets of differential equations for the wavevectors \vec{k}_ν and amplitudes A_ν of periodic functions. If w represents the normal deflection of the buckling plant tunica (in the biophysical model) or auxin concentration (in a biochemical model), we explain how the equation

$$w_t = \nabla^4 w + P \nabla^2 w + \Lambda^4 w + \text{nonlinear terms}, \quad (14)$$

for constants P and Λ^4 , captures both models. The linear terms are similar in both models, whereas the nonlinear terms are very different. The parameter P is the control parameter, representing compressive stress in the biophysical model and the relative strength of auxin transport to diffusion in the biochemical model. For large enough P , the homogeneous solution $w = 0$ becomes unstable to a solution that depends on both the nonlinear and linear terms in the equation. Depending on the nonlinear terms, the equation (14) may or may not be gradient (that is, the solution may or may not minimize an energy functional $\mathfrak{E}(w)$). The elastic energy plays the role of \mathfrak{E} for a mechanical buckling model. Whereas there there is no reason to assume that a biochemical mechanism would be gradient, an energy $\mathfrak{E}(w)$ may still be relevant near the threshold of pattern formation.

The ansatz is made that w is an \mathbb{L} -periodic function for some lattice \mathbb{L} with dual lattice \mathbb{K} , so that w has the form (5). The dual lattice vectors \vec{k}_m and \vec{k}_n can be functions of the spatial coordinates, so that \mathbb{L} should be viewed as a local lattice. For instance, when considering the function (5) in the plane, so that $\vec{x} = (s, \theta)$, wavevectors of the form (6) give a lattice in the plane, but translated to the disk, the appropriate expressions for the wavevectors have the form (9), where Γ is replaced by r , and the radial wavenumber depends on the radial coordinate. The spatial dependence can be more complex, so as to account for, for example, defects in the pattern. Here, however, we will only consider the very simplest case. Let us take $\vec{x} = (s, \theta)$ in (5), assume that our PDE model (14) has an energy $\mathfrak{E}(w)$, and make the ansatz that

$$w(s, \theta) = \sum_{\nu} A_{\nu} \cos(\vec{k}_{\nu} \cdot (s, \theta)) = \sum_{\nu} A_{\nu} \cos(l_{\nu}s + m_{\nu}\theta), \quad (15)$$

where $l_{\nu} = \frac{\Gamma}{g}(m_{\nu}d - q_{\nu})$. Minimization of $\mathfrak{E}(w)$ over functions of the form (15) then reduces to the minimization of an energy functional $\mathfrak{E}(\vec{k}_{\nu}; A_{\nu})$ over the wavevector sequence \vec{k}_{ν} and associated amplitudes A_{ν} . We calculate from a biophysical model in [28, 29] and from a biochemical model in [17] the energy

$$\begin{aligned} \mathfrak{E}(\vec{k}_{\nu}; A_{\nu}) = & - \sum_{\nu} \sigma(\vec{k}_{\nu}) A_{\nu} A_{\nu}^* - \sum \tau(\vec{k}_{\nu}, \vec{k}_p, \vec{k}_q) (A_{\nu} A_p A_q + A_{\nu}^* A_p^* A_q^*) \\ & + \gamma \left(\frac{1}{2} \sum_{\nu} A_{\nu-1}^2 A_{\nu-1}^{*2} + 2 \sum_{p \neq q} A_p A_p^* A_q A_q^* \right), \end{aligned} \quad (16)$$

where the cubic term is summed over all \vec{k}_p, \vec{k}_q in the sequences $\{\pm \vec{k}_{\nu}\}$ such that $\vec{k}_{\nu} + \vec{k}_p + \vec{k}_q = 0$. The important point to understand about (16) is that it is universal in form in that any system where triad interactions play an important role differs from (16) only in the coefficients σ, τ, γ . These coefficients contain the information specific to the microscopic mechanism under investigation and depend on the parameters in the original PDE as well as the wavevectors. The coefficient τ is calculated from the quadratic nonlinear terms in the PDE model. For example, our biophysical model [28, 29] yields a coefficient

$$\tau(\vec{k}_{\nu}, \vec{k}_p, \vec{k}_q) = C(l_p m_q - l_q m_p)^2 \sum_{j=\nu, p, q} \frac{1}{\|\vec{k}_j\|^2} = \frac{(2\pi)^2 C}{A} \sum_{j=\nu, p, q} \frac{1}{\|\vec{k}_j\|^2} = C(\mathcal{A}_{\nu} + \mathcal{A}_p + \mathcal{A}_q). \quad (17)$$

The parameter C (corresponding to curvature of the unbuckled surface in the mechanical model) measures the strength of the quadratic nonlinear terms in (14). For large C , triad interactions are important and lattice patterns are favored, whereas ridge-dominated planforms are favored for small C . Also, τ is maximized on those triads with largest \mathcal{A}_j , thus preferring the Voronoi tessellations as described in Section 3. If the system is isotropic, the coefficient $\sigma(\vec{k})$ of the quadratic term in (16) (calculated from the linear terms in (14)) evaluates the distance of a wavevector \vec{k} from the optimal length Λ , so that for $k^2 = \|\vec{k}\|^2$,

$$\sigma(\vec{k}) = -k^4 + Pk^2 - \Lambda^4 = (\text{for } P = 2\Lambda^2) - (k^2 - \Lambda^2)^2.$$

The energy (16) is taken to be a functional of only those modes for which $\sigma(\vec{k}_{\nu})$ is positive or slightly negative, say greater than a threshold σ_c . The wavevectors in the sequence \vec{k}_{ν} are parameterized by the four lattice constants A, Γ, d, g and the sequence m_{ν} . The radius R of the cylinder (or average radius of the generative region in case the pattern is forming on a non-cylindrical geometry) is an external parameter, not chosen by energy minimization, and the sequence m_{ν} determines g , so $\mathfrak{E}(\vec{k}_{\nu}, A_{\nu})$ can be treated as an energy

$\mathfrak{E}(A, d, m_\nu; A_\nu)$. If the coefficient τ is independent of A , as in (17), the optimal choice of A maximizes the coefficients $\sigma(\vec{k}_\nu)$, and, depending on P , A is chosen so that $k_\nu^2 \simeq \Lambda^2$. So, we will treat the energy as a function $\mathfrak{E}(d; A_\nu)$ of d and the A_ν and find critical points for arbitrary sequence m_ν . If $\sigma(\vec{k}) > \sigma_c$ for only four wavevectors $\vec{k}_{\nu-1}, \vec{k}_\nu, \vec{k}_{\nu+1}, \vec{k}_{\nu+2}$, the energy $\mathfrak{E}(d; A_{\nu-1}, A_\nu, A_{\nu+1}, A_{\nu+2})$ is a function of four amplitudes, and the equations that we need to solve read

$$-\frac{\partial \mathfrak{E}}{\partial d} = \sum -\frac{m_\nu}{g}(m_\nu d - q_\nu) \frac{\Gamma^2}{g}(4k_\nu^2 - 2P)A_\nu A_\nu^* \quad (18.a)$$

$$-\frac{\partial}{\partial d} \tau_1(A_{\nu-1}A_\nu A_{\nu+1} + A_{\nu-1}^* A_\nu^* A_{\nu+1}^*) - \frac{\partial}{\partial d} \tau_2(A_\nu A_{\nu+1} A_{\nu+2} + A_\nu^* A_{\nu+1}^* A_{\nu+2}^*) = 0,$$

$$-\frac{\partial \mathfrak{E}}{\partial A_{\nu-1}^*} = \sigma(k_{\nu-1}^2)A_{\nu-1} + \tau_1 A_\nu^* A_{\nu+1}^* - \gamma A_{\nu-1}(A_{\nu-1} A_{\nu-1}^* + 2 \sum_{p \neq \nu-1} A_p A_p^*) = 0, \quad (18.b)$$

$$-\frac{\partial \mathfrak{E}}{\partial A_\nu^*} = \sigma(k_\nu^2)A_\nu + \tau_1 A_{\nu-1}^* A_{\nu+1}^* + \tau_2 A_{\nu+1}^* A_{\nu+2}^* - \gamma A_\nu(A_\nu A_\nu^* + 2 \sum_{p \neq \nu} A_p A_p^*) = 0, \quad (18.c)$$

$$-\frac{\partial \mathfrak{E}}{\partial A_{\nu+1}^*} = \sigma(k_{\nu+1}^2)A_{\nu+1} + \tau_1 A_{\nu-1}^* A_\nu^* + \tau_2 A_\nu^* A_{\nu+2}^* - \gamma A_{\nu+1}(A_{\nu+1} A_{\nu+1}^* + 2 \sum_{p \neq \nu+1} A_p A_p^*) = 0 \quad (18.d)$$

$$-\frac{\partial \mathfrak{E}}{\partial A_{\nu+2}^*} = \sigma(k_{\nu+2}^2)A_{\nu+2} + \tau_2 A_\nu^* A_{\nu+1}^* - \gamma A_{\nu+2}(A_{\nu+2} A_{\nu+2}^* + 2 \sum_{p \neq \nu+2} A_p A_p^*) = 0, \quad (18.e)$$

where $\tau_1 = \tau(\vec{k}_{\nu-1}, \vec{k}_\nu, \vec{k}_{\nu+1})$, and $\tau_2 = \tau(\vec{k}_\nu, \vec{k}_{\nu+1}, \vec{k}_{\nu+2})$, and the quartic coefficient γ in (16) is taken to be constant (as it is in [28, 29]). Now let us see what happens when $\Gamma = \Gamma_{\nu,S} = \sqrt{m_\nu^2 + m_{\nu+1}^2}$. As calculated in Section 2.5, for $d = \tilde{d} = \frac{q_\nu m_\nu + q_{\nu+1} m_{\nu+1}}{m_\nu^2 + m_{\nu+1}^2}$, $\vec{\omega}_\nu$ and $\vec{\omega}_{\nu+1}$ are of equal length and orthogonal to each other, implying that $\vec{\omega}_{\nu-1}$ and $\vec{\omega}_{\nu+2}$ are also of equal length. Similar statements hold true for the corresponding wavevectors \vec{k}_ν and $\vec{k}_{\nu+1}$, and $\vec{k}_{\nu-1}$ and $\vec{k}_{\nu+2}$. Since σ is a function of the wavevector lengths, this means that $\sigma(\vec{k}_\nu) = \sigma(\vec{k}_{\nu+1})$, and $\sigma(\vec{k}_{\nu-1}) = \sigma(\vec{k}_{\nu+2})$. This indicates that we can find a solution of the system (18) with $A_\nu = A_{\nu+1} \in \mathbb{R}$ and $A_{\nu-1} = A_{\nu+2} \in \mathbb{R}$ and reduce the system to

$$\begin{aligned} 0 = & - \left(\frac{m_{\nu-1}}{g}(m_{\nu-1} \tilde{d} - q_{\nu-1}) + \frac{m_{\nu+2}}{g}(m_{\nu+2} \tilde{d} - q_{\nu+2}) \right) \frac{\Gamma^2}{g}(4k_{\nu-1}^2 - 2P)A_{\nu-1}^2 \\ & - \left(\frac{m_\nu}{g}(m_\nu \tilde{d} - q_\nu) + \frac{m_{\nu+1}}{g}(m_{\nu+1} \tilde{d} - q_{\nu+1}) \right) \frac{\Gamma^2}{g}(4k_\nu^2 - 2P)A_\nu^2 \\ & - 2C \frac{\Gamma^2}{g} \left[\left(\frac{m_{\nu-1}}{g}(m_{\nu-1} \tilde{d} - q_{\nu-1}) + \frac{m_{\nu+2}}{g}(m_{\nu+2} \tilde{d} - q_{\nu+2}) \right) A_{\nu-1}^2 \right. \\ & \left. - 2 \left(\frac{m_\nu}{g}(m_\nu \tilde{d} - q_\nu) + \frac{m_{\nu+1}}{g}(m_{\nu+1} \tilde{d} - q_{\nu+1}) \right) A_\nu^2 \right] A_{\nu-1} A_\nu^2, \end{aligned} \quad (19.a)$$

$$0 = \sigma(k_{\nu-1}^2)A_{\nu-1} + \tau_1 A_\nu^2 - \gamma A_{\nu-1}(A_{\nu-1}^2 + 2 \sum_{p \neq \nu-1} A_p^2), \quad (19.b)$$

$$0 = \sigma(k_\nu^2)A_\nu + \tau_1 A_{\nu-1} A_\nu + \tau_2 A_\nu A_{\nu-1} - \gamma A_\nu(A_\nu^2 + 2 \sum_{p \neq \nu} A_p^2), \quad (19.c)$$

where for $\frac{\partial}{\partial d} \tau$ in (18.a), we have used the expression for τ given by (17) in (19.a). But look at equation (19.a). We know that $\tilde{d} \simeq \hat{d}$, and from Proposition 2 have that $\frac{m_\nu}{g}(m_\nu \hat{d} - q_\nu) + \frac{m_{\nu+1}}{g}(m_{\nu+1} \hat{d} - q_{\nu+1}) \simeq \frac{1}{\sqrt{5}} - \frac{1}{\sqrt{5}} = 0$. In fact, it holds that $\frac{m_{\nu-1}}{g}(m_{\nu-1} \tilde{d} - q_{\nu-1}) + \frac{m_{\nu+2}}{g}(m_{\nu+2} \tilde{d} - q_{\nu+2}) = \frac{m_\nu}{g}(m_\nu \tilde{d} - q_\nu) + \frac{m_{\nu+1}}{g}(m_{\nu+1} \tilde{d} - q_{\nu+1}) = 0$, so that (19.a) vanishes for any $A_{\nu-1}, A_\nu$. The equations (19.b,c) are then easily solved for $A_{\nu-1}, A_\nu \in \mathbb{R}$. Since $\sigma(\vec{k}_{\nu-1}) < \sigma(\vec{k}_\nu)$, and due to the fact that A_ν is part of two triads (so that two quadratic terms appear in (19.c)), we obtain $A_{\nu-1} = A_{\nu+2} < A_\nu = A_{\nu+1}$, in accordance with the Fourier results of Fig. 4 for $\Gamma = \Gamma_{\nu,S}$. This critical point gives a minimum of $\mathfrak{E}(d, A_\nu)$ for values of the parameters for which τ is large relative to σ ; otherwise a single-roll solution with only one nonzero amplitude is the optimal configuration. The situation is similar when more than four amplitudes are included in the equations (18); the equation for d vanishes and the remaining (even number) of equations can be reduced by half so that $A_{\nu-n} = A_{\nu+n+1}$.

For $\Gamma \neq \Gamma_{\nu,S}$, it is more difficult to solve the system (18) analytically, but in [29] we solve the system numerically. The results of Section 1 entered here in the calculation of the value of d to minimize the energy, but they also indicate that a self-similar solution of the amplitude equations or the equation (14) itself, analogous to the function $\hat{\mathcal{A}}(\nu, \Gamma)$, may be analytically calculable. The curve $\mathcal{A}(\nu, \Gamma)$ has been derived in the previous sections from purely geometric considerations. A PDE-derived curve is not likely to have exactly the same shape as $\hat{\mathcal{A}}(\nu, \Gamma)$, and its height, width and overall shape will depend on the physical parameters in the model. The implications of such variations on the tiling shapes produced remain to be studied, but in [17] we show how the variation between square and diamond patterns, as described here in Section 3.5 with the parameter A' , can be achieved through the combined effects of biochemical and biomechanical mechanisms in a PDE model.

5 Conclusion

Spiral patterns of Fibonacci-like sequences are one of a number of arrangements observed on plants, and an idealization of these patterns, produced by searching for self-similarity and invariance, has been the subject of this paper. We conclude by discussing how the techniques described might be extended to capture a broader range of patterns and used to analyze real meristems.

As previously noted, the lattice parameter d is not typically constant, but rather varies as the phyllotactic pattern develops. This parameter is difficult to measure to the accuracy needed to know how it might typically evolve, but in simulations such as those of Douady and Couder [6], rhombic lattices are typically preferred, so the d will evolve along a curve in the van Iterson diagram. Certainly, variations in the parameters of the physical process are also factors in the variation. In relation to the invariant curve $\hat{\mathcal{A}}(\rho)$, note that $\hat{\mathcal{A}}(\rho = \Gamma/m_\nu)$ is only approximately equal to the amplitude $\hat{\mathcal{A}}_\nu(\Gamma)$. One may ask then, for a given value of Γ , what value of d best places the numbers $\mathcal{A}_\nu(\Gamma)$ near the invariant curve $\hat{\mathcal{A}}(\rho)$ (for example, in a least-squares sense). The values of d thus chosen would still approach \hat{d} for increasing Γ , but not be constant.

To compare our geometric results with real meristems, it would be desirable to extend the results to phyllotactic patterns on spheres or otherwise curved apices that better model plant meristems than the planar annuli considered here. As noted in Section 3.5, the diamond shapes of Fig. 8 (c) do not completely cover the annulus. But, they do provide a better packing of the annulus than does a representation of the primordia by disks (as in van Iterson's model). The question then arises of exactly how well the various diamond shapes, as parameterized by A' , pack the annulus and how well analogous constructions could cover spheres.

The derivations in this paper have been motivated by consideration of the mature sunflower seed heads of Fig. 1. Very important from a biological perspective is further thought on the stage in primordium development that the discussion of shape presented here is physically relevant. How much do the shapes of primordia change from the time they form at the meristem to the mature stage? Some SEM images of sunflower meristems do show diamond shapes or hexagonal patterns [19], and similar structures are also seen in cactus meristems. But, in many plants shapes evolve as they mature, and in particular diamonds on cacti can evolve into hexagons. The challenge is to integrate an understanding of the growth processes with the geometric descriptions of the observed patterns and their evolution.

One feature of the transition from Sections 2 and 3, which focused on global self-similarity, to Section 4, where we found solutions for amplitudes at a fixed value of Γ , is the use of the quantities $m_\nu(m_\nu d - q_\nu)$ as motivated by Proposition 2. In this way, a global condition on self-similarity is related to a local symmetry condition. This is important for the genesis of globally self-similar structures since patterns such as those seen in Fig. 1 essentially form as a front that propagates from the edge of the disk to the center (so that Γ decreases with time for the sunflower), so that global self-similarity can only be achieved if it is favored locally as the front propagates. A similar situation of global self-similarity is apparent in many other natural structures, such as viral capsids, where a notion of objectivity favors self-similar structures [12].

Finally, although we have focused on self-similar patterns and noble divergence angles, we should not forget that other patterns are also observed in nature. In fact, even rational values of d , such as the value $d = \frac{3}{8}$ whose lattice is pictured in Fig. 2, are common on many succulents. Rational values of d are also found in whorled patterns, as in decussate phyllotaxis. In [29], we discuss from the viewpoint of PDE models how anisotropies in the physical parameters can favor rational divergence angles and transitions between patterns that display defects. In future work, these patterns, as well as related ridge-dominated planforms, will be analyzed with Voronoi mountain functions under varying metrics.

Acknowledgments

This work has been motivated by collaboration and many discussions with Alan Newell. Thanks also to Dominik Freche and Jeff Ovall for discussions, Dick James for pointing out the connections to continued fraction expansions and the motivation for Proposition 2, Michael Shipman for help in casting Fig. 9, and to Todd Cooke and Jacques Dumais for lots of botanical advice. The work has been supported by NSF Grant No. DMS-0503196.

References

- [1] Atela, P., Golé, C., Hotton, S.: A dynamical system for plant pattern formation: Rigorous analysis. *J. Nonlinear Sci.* 12 (6), DOI 10.1007/s00332-002-0513-1 (2002)
- [2] Bravais, I., Bravais, A.: Essai sur la disposition des feuilles curvisériées. *Annales des Sciences Naturelles Botanique* 7, 42-110; 193-221; 8, 11-42 (1837)
- [3] Church, A. H.: On the Relation of Phyllotaxis to Mechanical Laws. Williams and Norgate (1904)
- [4] Dixon, R.: The shape of Dirichlet regions in a Coxeter lattice as a function of divergence and rise. Chapter 13, 213-333 of Jean, R.V., Barabé, Eds.: *Symmetry in Plants*. World Scientific (1998)
- [5] Douady, S.: The selection of phyllotactic patterns. Chapter 14, pg. 335-358, of Jean, R.V., Barabé, Eds.: *Symmetry in Plants*. World Scientific (1998)
- [6] Douady, S., Couder, Y.: Phyllotaxis as a dynamical self-organizing process, Part I: The spiral modes resulting from time-periodic iterations. *J. Theor. Biol.* 178, 255-274 (1996)
- [7] Douady, S., Couder, Y.: Phyllotaxis as a dynamical self-organizing process, Part II: The spontaneous formation of a periodicity and the coexistence of spiral and whorled patterns. *J. Theor. Biol.* 178, 295-312 (1996)
- [8] Gollwitzer, C., Rehberg, I., Richter, R.: Via hexagons to squares in ferrofluids: Experiments on hysteretic surface transformations under variation of the normal magnetic field. *Journal of Physics: Condensed Matter* 18 , S2643-S2656 (2006)
- [9] Green, P. B.: Expression of patterns in plants: Combining molecular and calculus-based paradigms. *Am. J. Botany* 86 (1999)
- [10] Hardy, G. H., Wright, E. M.: *An Introduction to the Theory of Numbers*, 5th Edition. Clarendon Press (1979)
- [11] Hotton, S., Johnson, V., Wilbarger, J., Zwieniecki, K., Atela, P., Golé, C., Dumais, J.: The possible and the actual in phyllotaxis: Bridging the gap between experimental observations and iterative models. *J. Plant Growth Reg.* 25, 313-323 (2006)
- [12] James, R. D.: Objective structures. *Journal of the Mechanics and Physics of Solids* 54, 2354-2390 (2006)
- [13] Jean, R. V.: *Phyllotaxis: A Systematic Study in Plant Morphogenesis*. Cambridge UP (1994)
- [14] Kelly, W. J., Cooke, T. J.: Geometrical relationships specifying the phyllotactic pattern of aquatic plants. *Am. J. Botany* 90 (8), 1131-1143 (2003)
- [15] Krantz, W. B., Gleason, K. J., Caine, N.: Patterned ground. *Scientific American* 259 (6), 44 (1988)
- [16] Newell, A. C., Shipman, P. D.: Plants and Fibonacci. *J. Stat. Phys.* 121 (5-6), 937-968 (2005)
- [17] Newell, A. C., Shipman, P. D., Sun, Z.: Phyllotaxis: Cooperation and competition between biophysical and biochemical processes. Submitted (2007)
- [18] Ocelli, R.: Transitions order-désordre dans les structures convectiones bi-dimensionnelles. Doctoral Thesis, Univ. of Provence, Marseille (1985)

- [19] Palmer, J. H.: The physiological basis of pattern generation in the sunflower. Chapter 7, 145-169 of Jean, R. V., Barabé, D., Eds. *Symmetry in Plants*. World Scientific (1998)
- [20] Reinhardt, D., Mandel, T., Kuhlemeier, C.: Auxin regulates the initiation and radial position of lateral organs. *Plant Cell* 12, 501-518 (2000)
- [21] Reinhardt, D., Pesce, E.-R., Stieger, P., Mandel, T., Baltensperger, K., Bennett, M., Traas, J., Friml, J., Kuhlemeier, C.: Regulation of phyllotaxis by auxin polar transport. *Nature* 426, 255-260 (2003)
- [22] Ridley, J. N.: Packing efficiency in sunflower heads. *Math. Biosci.* 585, 129-39 (1982a)
- [23] Richards, F. J.: Phyllotaxis: Its quantitative expression and relation to growth in the apex. *Phil. Trans. R. Soc. B* 235, 509-64 (1951)
- [24] Rivier, N., Occelli, R., Pantaloni, J., Lissowski, A.: Structure of Bénard convection cells, phyllotaxis, and crystallography in cylindrical symmetry. *J. Phys.* 45, 49-63 (1985)
- [25] Rivier, N.: A botanical quasicrystal. *J. Phys. France. Colloque C3 Suppl.* 7 (47), 299-309 (1986)
- [26] Rivier, H.: Crystallography of spiral lattices. *Mod. Phys. Lett. B* 2, 953-960 (1988)
- [27] Rothen, F., Koch, A. J.: Phyllotaxis, or the properties of spiral lattices. I. Shape invariance under compression. *J. Phys. France* 50, 633-57 (1989)
- [28] Shipman, P. D., Newell, A. C.: Phyllotactic patterns on plants. *Phys. Rev. Lett* 92 (16), 168102 (2004)
- [29] Shipman, P. D., Newell, A. C.: Polygonal planforms and phyllotactic patterns on plants. *J. Theor. Biol.* 236, 154-197 (2005)
- [30] van Iterson, G.: *Mathematische und mikroskopisch-anatomische Studien ueber Blattstellungen*. Verlag von Gustav Fischer. Jena (1907)
- [31] Williams, R. F.: *The Shoot Apex and Leaf Growth*, Cambridge UP, Cambridge (1975)